



1 **Development and evaluation of the interactive Model for Air Pollution and Land**

2 **Ecosystems (iMAPLE) version 1.0**

3

4 Xu Yue<sup>1#</sup>, Hao Zhou<sup>1#</sup>, Chenguang Tian<sup>1</sup>, Yimian Ma<sup>2</sup>, Yihan Hu<sup>1</sup>, Cheng Gong<sup>2</sup>, Hui  
5 Zheng<sup>3</sup>, Hong Liao<sup>1</sup>

6

7 <sup>1</sup>Jiangsu Key Laboratory of Atmospheric Environment Monitoring and Pollution  
8 Control, Collaborative Innovation Center of Atmospheric Environment and Equipment  
9 Technology, School of Environmental Science and Engineering, Nanjing University of  
10 Information Science & Technology (NUIST), Nanjing, 210044, China

11 <sup>2</sup> Department Biogeochemical Integration, Max Planck Institute for Biogeochemistry,  
12 Jena, 07745, Germany

13 <sup>3</sup> Key Laboratory of Regional Climate-Environment Research for Temperate East Asia,  
14 Institute of Atmospheric Physics, Chinese Academy of Sciences, Beijing, 100029,  
15 China

16

17

18 Corresponding authors: Xu Yue ([yuexu@nuist.edu.cn](mailto:yuexu@nuist.edu.cn))

19 Hong Liao ([hongliao@nuist.edu.cn](mailto:hongliao@nuist.edu.cn))

20

21

22 <sup>#</sup> These authors contribute equally

23



24 **Abstract**  
25 Land ecosystems are important sources and sinks of atmospheric components. In turn,  
26 air pollutants affect the exchange rates of carbon and water fluxes between ecosystems  
27 and atmosphere. However, these biogeochemical processes are usually not well  
28 presented in the Earth system models, limiting the explorations of interactions between  
29 land ecosystems and air pollutants from the regional to global scales. Here, we develop  
30 and validate the **interactive Model for Air Pollution and Land Ecosystems (iMAPLE)**  
31 by upgrading the Yale Interactive terrestrial Biosphere model with process-based water  
32 cycles, fire emissions, wetland methane (CH<sub>4</sub>) emissions, and the trait-based ozone (O<sub>3</sub>)  
33 damages. Within the iMAPLE, soil moisture and temperature are dynamically  
34 calculated based on the water and energy balance in soil layers. Fire emissions are  
35 dependent on dryness, lightning, population, and fuel load. Wetland CH<sub>4</sub> is produced  
36 but consumed through oxidation, ebullition, diffusion, and plant-mediated transport.  
37 The trait-based scheme unifies O<sub>3</sub> sensitivity of different plant functional types (PFTs)  
38 with the leaf mass per area. Validations show correlation coefficients (*R*) of 0.59-0.86  
39 for gross primary productivity (GPP) and 0.57-0.84 for evapotranspiration (ET) across  
40 the six PFTs at 201 flux tower sites, and yield an average *R* of 0.68 for CH<sub>4</sub> emissions  
41 at 44 sites. Simulated soil moisture and temperature match reanalysis data with the high  
42 *R* above 0.86 and low normalized mean biases (NMB) within 7%, leading to reasonable  
43 simulations of global GPP (*R*=0.92, NMB=1.3%) and ET (*R*=0.93, NMB=-10.4%)  
44 against satellite-based observations for 2001-2013. The model predicts an annual global  
45 area burned of 507.1 Mha, close to the observations of 475.4 Mha with a spatial *R* of  
46 0.66 for 1997-2016. The wetland CH<sub>4</sub> emissions are estimated to be 153.45 Tg [CH<sub>4</sub>]  
47 yr<sup>-1</sup> during 2000-2014, close to the multi-model mean of 148 Tg [CH<sub>4</sub>] yr<sup>-1</sup>. The model  
48 also shows reasonable responses of GPP and ET to the changes in diffuse radiation, and  
49 yields a mean O<sub>3</sub> damage of 2.9% to global GPP. The iMAPLE provides an advanced  
50 tool for studying the interactions between land ecosystem and air pollutants.

51  
52 **Keywords:** carbon fluxes, water cycle, fire emissions, methane emissions, ozone  
53 damage, diffuse radiation.



54 **1. Introduction**

55 As an important component on the Earth, land ecosystems regulate global carbon and  
56 water cycles. Every year, the ecosystem assimilates  $\sim 120$  Pg ( $1 \text{ Pg} = 10^{15} \text{ g}$ ) carbon  
57 from atmosphere through vegetation photosynthesis (Beer et al., 2010). However, most  
58 of these carbon uptake returns to atmosphere due to plant and soil respirations (Sitch et  
59 al., 2015), as well as other perturbations such as biomass burning and biogenic  
60 emissions (Carslaw et al., 2010; van der Werf et al., 2010), leading to a net carbon sink  
61 of only  $\sim 2$  Pg C yr<sup>-1</sup> (Friedlingstein et al., 2022). Meanwhile, land ecosystems affect  
62 atmospheric moisture and soil wetness through both physical (e.g., evaporation and  
63 runoff) and physiological (e.g., leaf transpiration and root hydrological uptake)  
64 processes. Observations show that transpiration accounts for 80%-90% of the terrestrial  
65 evapotranspiration (ET) (Jasechko et al., 2013) and makes significant contributions to  
66 land precipitation especially over the tropical forests (Spracklen et al., 2012).

67

68 Different approaches have been applied to depict the spatiotemporal variations of  
69 ecosystem processes. The eddy covariance technique provides direct measurements of  
70 land carbon and water fluxes (Jung et al., 2011). However, the limited number and  
71 uneven distribution of ground sites results in large uncertainties in the upscaling of site-  
72 level fluxes to the global scale (Jung et al., 2020b). Satellite retrieval provides a unique  
73 tool for the continuous representations of land fluxes in both space and time (Worden  
74 et al., 2021). However, most of the ecosystem variables (e.g., gross primary productivity,  
75 GPP) can only be derived using available signals from remote sensing through  
76 empirical relationships (Madani et al., 2017). As a comparison, process-based models  
77 build physical parameterizations based on field and/or laboratory experiments and  
78 validate against the available *in situ* and satellite-based observations (Niu et al., 2011;  
79 Castillo et al., 2012). These models can be further applied at different spatial (from site  
80 to global) and temporal (from days to centuries) scales to identify the main drivers of  
81 the changes in carbon and water fluxes (Sitch et al., 2015). For example, a total of 17  
82 vegetation models were validated and combined to predict the land carbon fluxes in the



83 past century (Friedlingstein et al., 2022); the ensemble mean of these models revealed  
84 a steadily increasing land carbon sink from 1960 with the dominant contribution by  
85 CO<sub>2</sub> fertilization.

86  
87 While many studies quantified the ecosystem responses to the effects of CO<sub>2</sub>, climate,  
88 and human activities (Piao et al., 2009; Sitch et al., 2015), few have explored the  
89 interactions between air pollution and land ecosystems. Such biogeochemical processes  
90 become increasingly important in the Anthropocene period with significant changes in  
91 atmospheric compositions. For example, observations found that nitrogen and  
92 phosphorus constrain the CO<sub>2</sub> fertilization efficiency of global vegetation (Terrer et al.,  
93 2019), but such limiting effect is ignored or underestimated in most of the current  
94 models (Wang et al., 2020). Tropospheric ozone (O<sub>3</sub>) damages plant photosynthesis and  
95 stomatal conductance, inhibiting carbon assimilation and the ET from the land surface  
96 (Sitch et al., 2007; Lombardozzi et al., 2015). Atmospheric aerosols can enhance  
97 photosynthesis through diffuse fertilization effects (Mercado et al., 2009) but  
98 meanwhile decrease photosynthesis by reducing precipitation (Yue et al., 2017). In turn,  
99 ecosystems act as both the sources and sinks of atmospheric components. Biomass  
100 burning emits a large amount of carbon dioxide, trace gases, and particulate matters,  
101 further influencing air quality (Chen et al., 2021), ecosystem functions (Yue and Unger,  
102 2018), and global climate (Tian et al., 2022). Biogenic volatile organic compounds  
103 (BVOCs) are important precursors for both surface O<sub>3</sub> and secondary organic aerosols  
104 (Wu et al., 2020), which can feed back to affect biogenic emissions (Yuan et al., 2016)  
105 and carbon assimilations (Rap et al., 2018). Wetland methane (CH<sub>4</sub>) emissions account  
106 for the dominant fraction of natural sources of CH<sub>4</sub>, and are projected to increase under  
107 the global warming scenarios (Zhang et al., 2017; Rosentreter et al., 2021). On the other  
108 hand, stomatal uptake dominates the dry deposition of air pollutants over the vegetated  
109 land (Lin et al., 2020). Meanwhile, ET from forest results in the increase of water vapor  
110 in atmosphere (Spracklen et al., 2012), affecting the consequent rainfall and wet  
111 deposition of particles.



112

113 Currently, numerical models are in general developed separately for atmospheric  
114 chemistry and ecosystem processes. The chemical transport models are usually driven  
115 with prescribed emissions of biomass burning (Warneke et al., 2023) and wetland  
116 methane (Heimann et al., 2020), while the ecosystem models often ignore the  
117 biogeochemical impacts of O<sub>3</sub> and aerosols (Friedlingstein et al., 2022). In an earlier  
118 study, we developed and validated the Yale Interactive terrestrial Biosphere (YIBs)  
119 model version 1.0 with the special focus on the interactions between atmospheric  
120 chemistry and land ecosystems (Yue and Unger, 2015). Thereafter, the YIBs model has  
121 been used offline to assess the O<sub>3</sub> vegetation damage (Yue et al., 2016), aerosol diffuse  
122 fertilization (Yue and Unger, 2017), BVOCs emissions (Cao et al., 2021a), as well as  
123 coupled to other models to investigate the carbon-chemistry-climate interactions (Lei  
124 et al., 2020; Gong et al., 2021). The YIBs model has joined the multi-model  
125 intercomparison project of TRENDY since the year 2020 and showed reasonable  
126 performance in the simulation of carbon fluxes (Friedlingstein et al., 2020). However,  
127 the YIBs model failed to predict the typical hydrological variables such as ET and  
128 runoff due to the missing of carbon-water coupling modules. Furthermore, the model  
129 did not consider the nutrient limitation on plant photosynthesis and ignored some key  
130 exchange fluxes between land and atmosphere.

131

132 In this study, we develop the interactive **Model for Air Pollution and Land Ecosystems**  
133 (iMAPLE) by coupling the process-based water cycle module from Noah-MP (Niu et  
134 al., 2011) to the carbon cycle in the YIBs (Figure 1). In addition, we update the original  
135 YIBs model with some major advances in the biogeochemical processes including  
136 dynamic fire emissions, wetland CH<sub>4</sub> emissions, nutrient limitations on photosynthesis,  
137 and the trait-based O<sub>3</sub> vegetation damage. The detailed descriptions of these updates  
138 are presented in the next section. The iMAPLE is fully validated against available  
139 measurements in Section 3. The last section will summarize the model performance and  
140 rethink the prospective directions for future development.



141

## 142 **2. Models and data**

### 143 **2.1 Main features of YIBs model**

144 The YIBs model is a process-based vegetation model predicting land carbon fluxes with  
145 dynamic changes in tree height, leaf area index, and carbon pools (Yue and Unger, 2015,  
146 thereafter YU2015). A total of nine plant functional types (PFTs) are considered  
147 including evergreen broadleaf forest (EBF), evergreen needleleaf forest (ENF),  
148 deciduous broadleaf forest (DBF), tundra, shrubland, C<sub>3</sub>/C<sub>4</sub> grassland, and C<sub>3</sub>/C<sub>4</sub>  
149 cropland. Leaf photosynthesis is calculated using the well-established Michaelis-  
150 Menten enzyme-kinetics scheme (Farquhar et al., 1980) and is coupled to stomatal  
151 conductance with the modulations of air humidity and CO<sub>2</sub> concentrations (Ball et al.,  
152 1987). The model applies a two-leaf approach to distinguish the irradiating states for  
153 sunlit and shading leaves and adopts an adaptive stratification for the radiative transfer  
154 processes within canopy layers (Spitters, 1986). The gross carbon assimilation is further  
155 regulated by the optimized plant phenology, which is mainly dependent on temperature  
156 and light for deciduous trees (Yue et al., 2015) but temperature and/or moisture for  
157 shrubland and grassland (YU2015). The assimilated carbon is allocated among leaf,  
158 stem, and root to support autotrophic respiration and development, the latter of which  
159 is used to update plant height and leaf area (Cox, 2001). The input of litterfall triggers  
160 the carbon transition among 12 soil carbon pools and determines the magnitude of  
161 heterotrophic respiration with the joint effects of soil temperature, moisture, and texture  
162 (Schaefer et al., 2008). The net carbon uptake is then calculated by subtracting  
163 ecosystem respiration (plant and soil) and environmental perturbations (reforestation or  
164 deforestation) from the gross carbon assimilation (Yue et al., 2021). The YIBs model  
165 reasonably reproduces the observed spatiotemporal patterns of global carbon fluxes and  
166 makes contributions to the Global Carbon Project with the long-term simulations of  
167 land carbon sink in the past century (Friedlingstein et al., 2020). The model specifically  
168 considers air pollution impacts on land ecosystems (Figure 1), such as the ozone  
169 vegetation damage (Yue and Unger, 2014) and aerosol diffuse fertilization effect (Yue



170 and Unger, 2017). The YIBs implements two different schemes for BVOCs emissions  
171 (Figure 1), including the Model of Emissions of Gases and Aerosols from Nature  
172 (MEGAN, Guenther et al., 2012) and the photosynthesis-dependent (PS\_BVOC)  
173 scheme (Unger et al., 2013).

174

## 175 **2.2 New processes in iMAPLE model**

### 176 2.2.1 Process-based water cycles

177 We implement the hydrological module from Noah-MP into the iMAPLE model (Niu  
178 et al., 2011). The water budget closure is achieved by constructing water-balance  
179 equations among precipitation ( $P$ ,  $\text{Kg m}^{-2} \text{s}^{-1}$ ), evapotranspiration ( $ET$ ,  $\text{Kg m}^{-2} \text{s}^{-1}$ ),  
180 runoff, and terrestrial water storage change ( $\Delta TWS$ ) on each grid cell as follows:

$$181 \quad P = ET + runoff + \Delta TWS \quad (1)$$

182 Here, hourly  $P$  from MERRA-2 reanalyses is used as the input.

183

184 We then divide  $ET$  into three portions including plant transpiration ( $TRA$ ), canopy  
185 evaporation ( $ECAN$ ) and ground evaporation ( $EGRO$ ):

$$186 \quad ET = TRA + ECAN + EGRO \quad (2)$$

187 For vegetated grids,  $TRA$  is calculated as follows:

$$188 \quad TRA = \frac{\rho_{air} \cdot CP_{air} \cdot C_{tra} \cdot (e_{sat} - e_{ca})}{PC} \quad (3)$$

189 where  $\rho_{air}$  is air density,  $CP_{air}$  is heat capacity of dry air, and  $PC$  is the  
190 psychrometric constant.  $e_{sat}$  is the saturated vapor pressure at the leaf temperature,  
191  $e_{ca}$  is the vapor pressure of the canopy air and  $C_{tra}$  is leaf transpiration conductance,  
192 which is calculated based on the Ball-Berry scheme of stomatal resistance (Yue and  
193 Unger, 2015).

194

195 Runoff includes surface ( $R_{srf}$ ) and subsurface ( $R_{sub}$ ) components:

$$196 \quad runoff = R_{srf} + R_{sub} \quad (4)$$

197 The surface runoff is calculated as follows:

$$198 \quad R_{srf} = Q_{soil,srf} - Q_{soil,in} \quad (5)$$



199 where  $Q_{soil,srf}$  is the incident water in the soil surface and is the sum of the  
200 precipitation, snowmelt and dewfall. Here, we assume independent and exponential  
201 distributions of infiltration capacity and precipitation in each grid cell when considering  
202 soil infiltration processes and  $Q_{soil,in}$  is the infiltration into the soil, following the  
203 approach by Schaake et al. (1996). We assume free drainage processes in the soil  
204 column bottom, thus the  $R_{sub}$  is calculated as follows:

$$205 \quad R_{sub} = \alpha_{slope} \cdot K_4 \quad (6)$$

206 where  $\alpha_{slope} = 0.1$  is the terrain slope index.  $K_4$  is the hydraulic conductivity in the  
207 bottom soil layer from soil parameterizes used in Clapp and Hornberger (1978).

208

209 Terrestrial water storage ( $TWS$ ) is the sum of groundwater storage ( $W_{gw}$ ), soil water  
210 content ( $W_{soil}$ ) and snow water equivalent ( $W_{snow}$ ):

$$211 \quad TWS = W_{gw} + W_{snow} + \sum_{i=1}^{N_{soil}} W_{soil} \quad (7)$$

212 Here, the soil module includes four layers ( $N_{soil} = 4$ ) and  $W_s$  is calculated by the  
213 volumetric water content ( $W_i$ ) as follows:

$$214 \quad W_s = \rho_{wat} \cdot W_i \cdot \Delta Z_i \quad for \ i = 1, 2, 3, 4 \quad (8)$$

215 where water density ( $\rho_{wat}$ ) = 1000 kg m<sup>-3</sup>, and  $\Delta Z_i = 0.1, 0.3, 0.6$  and 1m, respectively.  
216 Hourly  $W_i$  depends on variations of soil water diffusion ( $D$ ) and hydraulic  
217 conductivity ( $K$ ) as follows:

$$218 \quad \frac{\partial W}{\partial t} = \frac{\partial}{\partial z} \left( D \frac{\partial W}{\partial z} \right) + \frac{\partial K}{\partial z} \quad (9)$$

219 Here,  $K$  and  $D$  are calculated following the parameterizations of Clapp-Hornberger  
220 curves (Clapp and Hornberger, 1978):

$$221 \quad \frac{K}{K_{sat}} = \left( \frac{W}{W_{sat}} \right)^{2b+3} \quad (10)$$

$$222 \quad D = K \cdot \frac{\partial \varphi}{\partial W} \quad (11)$$

$$223 \quad \frac{\varphi}{\varphi_{sat}} = \left( \frac{W}{W_{sat}} \right)^{-b} \quad (12)$$

224 where  $\varphi_{sat}$ ,  $W_{sat}$  and  $K_{sat}$  are saturated soil capillary potential, volumetric  
225 water content and hydraulic conductivity. Exponent  $b$  is an empirical constant



226 depending on soil types. Soil moisture is calculated as the ratio of  $W_s$  to  $W_{sat}$ .

227

228 Soil temperature ( $T_s$ ) is calculated through physical processes as follows:

$$229 \quad \frac{\partial T_s}{\partial t} = \frac{1}{c} \frac{\partial}{\partial z} \left( K_T \frac{\partial T_s}{\partial z} \right) \quad (13)$$

230 Here  $K_T$  is soil specific heat capacity:

$$231 \quad K_T = K_e \cdot (K_s - K_{dry}) + K_{dry} \quad (14)$$

232 where  $K_e$ ,  $K_s$  and  $K_{dry}$  are Kersten values as a function of soil wetness, saturated  
233 soil heat conductivity and that under dry air conditions (Niu et al., 2011).  $C$  in Equation  
234 (13) is the specific heat

$$235 \quad C = W_{lip} \cdot C_{lip} + W_{ice} \cdot C_{ice} + (1 - W_{sat}) \cdot C_{sat} + (W_{sat} - W) \cdot C_{air} \quad (15)$$

236 Here,  $W_{lip}$ ,  $C_{lip}$  and  $W_{ice}$ ,  $C_{ice}$  indicate water content and heat capacity on soil  
237 water and ice.  $C_{sat}$  and  $C_{air}$  are saturated and air heat capacity, which are empirical  
238 constants (Niu et al., 2011).

239

#### 240 2.2.2 Dynamic fire emissions

241 We implement the active global fire parameterizations from Pechony and Shindell  
242 (2009) and Li et al. (2012) to the iMAPLE model. The fire emissions are determined  
243 by several key factors such as fuel flammability, natural ignitions, human activities, and  
244 fire spread. The fire count  $N_{fire}$  depends on flammability ( $Flam$ ), fire ignition (including  
245 both natural ignition rate  $I_N$  and anthropogenic ignition rate  $I_A$ ) and anthropogenic  
246 suppression ( $F_{NS}$ ):

$$247 \quad N_{fire} = Flam \times (I_N + I_A) \times F_{NS} \quad (16)$$

248  $Flam$  is a unitless metric representing conditions conducive to fire occurrence. It is  
249 parameterized as a function of vapor pressure deficit (VPD), precipitation (Prec), and  
250 leaf area index (LAI):

$$251 \quad Flam = VPD \times e^{-2 \times Prec} \times LAI \quad (17)$$

252  $I_N$  depends on the cloud-to-ground lightning and  $I_A$  can be expressed as:

$$253 \quad I_A = 0.03 \times PD \times k(PD) \quad (18)$$

254 where  $PD$  is population density. The empirical function of  $k(PD) = 6.8 \times PD^{-0.6}$  stands



255 for ignition potentials by human activity. The fraction of non-suppressed fires  $F_{NS}$  is  
256 derived as:

$$257 \quad F_{NS} = 0.05 + 0.95 \times e^{-0.05 \times PD} \quad (19)$$

258

259 The burned area of a single fire ( $BA_{single}$ ) is typically taken to be elliptical in shape  
260 associated with near-surface wind speed ( $U$ ) and relative humidity ( $RH$ ):

$$261 \quad BA_{single} = \frac{\pi \times UP^2}{4 \times LB} \times \left(1 + \frac{1}{HB}\right)^2 \quad (20)$$

262 where  $LB$  and  $HB$  are length-to-breadth ratio and head-to-back ratio, respectively:

$$263 \quad LB = 1 + 10 \times (1 - e^{-0.06 \times U}) \quad (21)$$

$$264 \quad HB = \frac{LB + (LB^2 - 1)^{0.5}}{LB - (LB^2 - 1)^{0.5}} \quad (22)$$

265 The rate of fire spread ( $UP$ ) is computed as:

$$266 \quad UP = UP_{max} \times f_{RH} \times f_{\theta} \times G(W) \quad (23)$$

267 Here,  $UP_{max}$  is the maximum fire spread rate depending on PFTs,  $f_{\theta}$  is set to 0.5 and  
268  $f_{RH}$  is calculated as:

$$269 \quad f_{RH} = \begin{cases} 0, & RH \leq RH_{low} \\ \frac{RH_{up} - RH}{RH_{up} - RH_{low}}, & RH_{low} < RH < RH_{up} \\ 1, & RH \geq RH_{up} \end{cases} \quad (24)$$

270 In this study, we set  $RH_{low} = 30\%$  and  $RH_{up} = 70\%$ .  $G(W)$  is the limit of the fire spread:

$$271 \quad G(W) = \frac{LB}{1 + \frac{1}{HB}} \quad (25)$$

272

273 Finally, the burned area ( $BA$ ) is represented as:

$$274 \quad BA = BA_{single} \times N_{fire} \quad (26)$$

275 The fire-emitted trace gases and aerosols ( $Emis$ ) are calculated as:

$$276 \quad Emis = BA \times EF \quad (27)$$

277 where  $EF$  is the emission factors for different species (such as black carbon and organic  
278 carbon aerosols).

279

### 280 2.2.3 Wetland methane emissions

281 We implement the process-based wetland  $CH_4$  emissions into the iMAPLE model. For



282 each soil layer, the flux of  $\text{CH}_4$  ( $F_{\text{CH}_4}$ ) is calculated as the difference between production  
283 ( $P_{\text{CH}_4}$ ) and consumptions, which include oxidation ( $O_{\text{CH}_4}$ ), ebullition ( $E_{\text{CH}_4}$ ), diffusion  
284 ( $D_{\text{CH}_4}$ ), and plant-mediated transport through aerenchyma ( $A_{\text{CH}_4}$ ) as follows:

$$285 \quad F_{\text{CH}_4} = P_{\text{CH}_4} - O_{\text{CH}_4} - E_{\text{CH}_4} - D_{\text{CH}_4} - A_{\text{CH}_4} \quad (28)$$

286 The net methane emission to the atmosphere is the sum of ebullition, diffusion and  
287 aerenchyma transport from the top soil layer.

288

289 The production of  $\text{CH}_4$  in soil depends on the quantity of carbon substrate and  
290 environmental conditions including soil temperature  $T_s$ , pH, and wetland inundation  
291 fraction  $f_{\text{wetland}}$  as follows:

$$292 \quad P_{\text{CH}_4} = R_h r f_{T_s} f_{\text{pH}} f_{\text{wetland}} \quad (29)$$

293 where  $R_h$  is the heterotrophic respiration estimated at the grid cell ( $\text{mol C m}^{-2} \text{s}^{-1}$ ).  
294  $r$  represents the release ratio of methane and carbon dioxide (Wania et al., 2010). We  
295 determine the dependence on  $T_s$  and soil pH in iMAPLE based on the parameterizations  
296 from the TRIPLEX-GHG model (Zhu et al., 2014). For the temperature-dependence,  
297 the  $Q_{10}$  relationships are applied as follows:

$$298 \quad Q_{10} = r_b Q_b^{\frac{T_s - T_{\text{base}}}{10}} \quad (30)$$

299 Here  $r_b$  is set to 3.0 and  $Q_b$  is 1.33 with a base temperature ( $T_{\text{base}}$ ) of 25°C (Zhu et al.,  
300 2014; Paudel et al., 2016). The inundation fraction of wetland at each cell describes the  
301 proportion of anaerobic conditions (Zhang et al., 2021). We ignore the impact of redox  
302 potential (Eh) because global observations are not available and the Eh-related  
303 processes are poorly characterized in current models (Wania et al., 2010).

304

305 The oxidation of  $\text{CH}_4$  is a series of aerobic activities related to temperature and  $\text{CH}_4$   
306 concentrations:

$$307 \quad O_{\text{CH}_4} = [\text{CH}_4] f_{T_s} f_{\text{CH}_4} \quad (31)$$

308 where  $[\text{CH}_4]$  is the methane amount in each soil layer ( $\text{gC m}^{-2} \text{layer}^{-1}$ ).  $f_{\text{CH}_4}$  is the  
309  $\text{CH}_4$  concentration factor representing a Michaelis-Menten kinetic relationship:

$$310 \quad f_{\text{CH}_4} = \frac{[\text{CH}_4]}{[\text{CH}_4] + K_{\text{CH}_4}} \quad (32)$$



311 where  $K_{CH_4} = 5 \mu\text{mol L}^{-1}$  is the half-saturation coefficient with respect to  $\text{CH}_4$  (Walter  
312 and Heimann, 2000). For temperature-dependence of oxidation, the  $Q_{10}$  relationship  
313 with  $r_b = 2.0$ ,  $Q_b = 1.9$ , and  $T_{base} = 12^\circ\text{C}$  is adopted (Zhu et al., 2014; Paudel et al., 2016).  
314

315 The diffusion of  $\text{CH}_4$  follows the Fick's law with dependence on  $\text{CH}_4$  concentrations  
316 and the molecular diffusion coefficients of  $\text{CH}_4$  in the air ( $D_a = 0.2 \text{ cm}^2\text{s}^{-1}$ ) and water  
317 ( $D_w = 0.00002 \text{ cm}^2\text{s}^{-1}$ ) respectively (Walter and Heimann, 2000). For each soil layer  
318  $i$ , the diffusion coefficient  $D_i$  can be calculated as follows :

$$319 \quad D_i = D_a \times (R_{sand} \times 0.45 + R_{silt} \times 0.2 + R_{clay} \times 0.14) \times f_{tort} \times S_{poro} \times (1 - \\ 320 \quad WFPS_i) + D_w \times WFPS_i \quad (33)$$

321 where  $R_{sand}$ ,  $R_{silt}$ ,  $R_{clay}$  is the relative content of sand, silt, and clay in the soil,  
322  $f_{tort} = 0.66$  is tortuosity coefficient,  $S_{poro}$  is soil porosity, and  $WFPS$  represents the  
323 pore space full of water (Zhuang et al., 2004).  
324

325 The ebullition of  $\text{CH}_4$  occurs when  $\text{CH}_4$  concentration is above the threshold of  $0.5$   
326  $\text{mol CH}_4\text{m}^{-3}$  (Walter et al., 2001). Since the process of ebullition occurs in a very short  
327 time, the bubbles will generate at once and all the flux will be released to atmosphere  
328 if the concentration reaches the threshold. The plant-mediated transport of  $\text{CH}_4$  through  
329 aerenchyma is dependent on the concentration gradient of  $\text{CH}_4$  and the plant-related  
330 factors (Zhu et al., 2014).  
331

#### 332 2.2.4 The down regulation on photosynthesis

333 We implement the down regulation parameterization from Arora et al. (2009) to indicate  
334 the nutrient limitations on leaf photosynthesis. A down-regulating factor  $\varepsilon$  is calculated  
335 as a function of  $\text{CO}_2$  concentrations ( $C$ ) as follows:

$$336 \quad \varepsilon(C) = \frac{1 + \gamma_{gd} \ln(C/C_0)}{1 + \gamma_g \ln(C/C_0)} \quad (34)$$

337 where  $C_0$  is a reference  $\text{CO}_2$  concentration set to 288 ppm. The values of  $\gamma_{gd} = 0.42$  and  
338  $\gamma_g = 0.90$  are derived from multiple measurements to constrain the  $\text{CO}_2$  fertilization.  
339 Then the down-regulated photosynthesis is calculated by scaling the original value with



340 the factor of  $\varepsilon$ .

341

342 2.2.5 Trait-based O<sub>3</sub> vegetation damaging scheme

343 The YIBs model considers O<sub>3</sub> vegetation damage using the flux-based scheme proposed  
344 by Sitch et al. (2007) (thereafter S2007), which determines the damaging ratio  $F$  of  
345 plant photosynthesis as follows:

$$346 \quad F = a_{PFT} \times \max\{f_{O_3} - t_{PFT}, 0\} \quad (35)$$

347 Here, the  $f_{O_3}$  denotes O<sub>3</sub> stomatal flux (nmol m<sup>-2</sup> s<sup>-1</sup>) defined as:

$$348 \quad f_{O_3} = \frac{[O_3]}{r + \left[ \frac{k_{O_3}}{g_p \times (1-F)} \right]} \quad (36)$$

349 where  $[O_3]$  represents the O<sub>3</sub> concentrations at the reference level (nmol m<sup>-3</sup>).  $r$  is the  
350 sum of boundary and aerodynamic resistance between leaf surface and reference level  
351 (s m<sup>-1</sup>).  $g_p$  is the potential stomatal conductance for H<sub>2</sub>O (m s<sup>-1</sup>).  $k_{O_3} = 1.67$  is a  
352 conversion factor of leaf resistance for O<sub>3</sub> to that for water vapor. The level of O<sub>3</sub>  
353 damage is then determined by the PFT-specific sensitivity  $a_{PFT}$  and threshold  $t_{PFT}$ ,  
354 which are different among PFTs.

355

356 In iMAPLE, we implement the trait-based O<sub>3</sub> vegetation damaging scheme to unify the  
357 inter-PFT sensitivities (Ma et al., 2023):

$$358 \quad a_{PFT} = \frac{a}{LMA} \quad (37)$$

359 Here, a unified plant sensitivity  $a$  (nmol<sup>-1</sup> g s) is scaled by leaf mass per area (LMA, g  
360 m<sup>-2</sup>) to derive the sensitivity of a specific PFT ( $a_{PFT}$ ). Accordingly, the damaging  
361 fraction  $F$  is modified as follows:

$$362 \quad F = a \times \max\left\{ \frac{f_{O_3}}{LMA} - t, 0 \right\} \quad (38)$$

363 Here  $t$  (nmol g<sup>-1</sup> s<sup>-1</sup>) is a unified flux threshold for O<sub>3</sub> vegetation damage. The updated  
364 scheme considers the dilution effects of O<sub>3</sub> dose through leaf cross-section by  
365 incorporating LMA. Plants with high LMA (e.g., ENF and EBF) usually have low  
366 sensitivities, and those with low LMA (e.g., DBF and crops) are more sensitive to O<sub>3</sub>  
367 damages. The unified sensitivity  $a$  is set to 3.5 nmol<sup>-1</sup> g s and threshold  $t$  is set to 0.019



368 nmol g<sup>-1</sup> s<sup>-1</sup> by calibrating simulated *F* values with literature-based measurements (Ma  
369 et al., 2023).

370

### 371 **2.3 Design of simulations**

372 We perform four sensitivity experiments with the iMAPLE model. The baseline (BASE)  
373 simulation considers the two-way coupling between carbon and water cycles, so that  
374 the prognostic soil meteorology drives canopy photosynthesis and evapotranspiration.  
375 A sensitivity run named BASE\_NW is set up by turning off the water cycle in the  
376 iMAPLE model. In this simulation, the soil moisture and soil temperature are adopted  
377 from the Modern-Era Retrospective Analysis for Research and Applications, Version 2  
378 (MERRA-2) reanalyses (Gelaro et al., 2017). The third and fourth runs turn on the O<sub>3</sub>  
379 vegetation damage effect using either the LMA-based scheme (O3LMA) or the S2007  
380 scheme (O3S2007). For all simulations, the iMAPLE model is driven with the hourly  
381 surface meteorology at a spatial resolution of 1°×1° from the MERRA-2 reanalyses,  
382 including surface air temperature, air pressure, specific humidity, wind speed,  
383 precipitation, snowfall, shortwave and longwave radiation. We run the model for the  
384 period of 1980-2021 using the initial conditions of the equilibrium soil carbon pool,  
385 tree height, and water fluxes from a spin-up run of 200 years.

386

387 The iMAPLE model is driven with observed CO<sub>2</sub> concentrations from Mauna Loa  
388 (Keeling et al., 1976) and the land cover fraction of nine PFTs derived by combining  
389 satellite retrievals from both Moderate Resolution Imaging Spectroradiometer (MODIS)  
390 (Hansen et al., 2003) and Advanced Very High Resolution Radiometer (AVHRR)  
391 (Defries et al., 2000). For fire emissions, we use Gridded Population of the World  
392 version 4 (<https://sedac.ciesin.columbia.edu/data/collection/gpw-v4>) to calculate  
393 human ignition and suppression. The lightning ignition is calculated using the flash rate  
394 from Very High Resolution Gridded Lightning Climatology Data Collection Version 1  
395 ([https://ghrc.nsstc.nasa.gov/uso/ds\\_details/collections/lisvhrcC.html](https://ghrc.nsstc.nasa.gov/uso/ds_details/collections/lisvhrcC.html)). For wetland  
396 CH<sub>4</sub> emissions, we use the 2000-2020 global dataset of Wetland Area and Dynamics



397 for Methane Modeling (WAD2M) derived from static datasets and remote sensing  
398 (Zhang et al., 2021), global soil pH from Hengl et al. (2017), and gridded soil texture  
399 from Scholes et al. (2011). For the LMA-based O<sub>3</sub> damage scheme, we use gridded  
400 LMA derived from the trait-level dataset of TRY (Kattge et al., 2011) using the random  
401 forest model (Moreno-Martínez et al., 2018).

402

#### 403 **2.4 Data for validations**

404 We use observational datasets to validate the biogeochemical processes and related  
405 variables simulated by the iMAPLE model. For simulated carbon and water fluxes, site-  
406 level observations are collected from the 201 sites at the FLUXNET network (Table  
407 S1). We also use the global gridded observations of GPP from the satellite retrievals  
408 including the solar-induced chlorophyll fluorescence (SIF) product GOSIF (Li and  
409 Xiao, 2019) and the Global land surface satellite (GLASS) product (Yuan et al., 2010).  
410 The global observations of ET are adopted from the benchmark product of FLUXCOM  
411 (Jung et al., 2020a) and the satellite-based GLASS product. For the dynamic fire  
412 module, we use monthly observed area burned from the Global Fire Emission Database  
413 version 4.1 with small fires (GFED4.1s) during 1997-2016 (van der Werf et al., 2010;  
414 Randerson et al., 2012). For methane emissions, we use site-level measurements of CH<sub>4</sub>  
415 fluxes from the FLUXNET-CH<sub>4</sub> network (Delwiche et al., 2021). We exclude the  
416 monthly records with missing data at more than half of the days and calculate the long-  
417 term mean fluxes for the seasonal cycle. In total, we select 44 sites with at least six  
418 months of data available for the validations (Table S2). We also use the anthropogenic  
419 sources of CH<sub>4</sub> from the archive of Coupled Model Intercomparison Project phase 6  
420 (CMIP6, <https://esgf-node.llnl.gov/projects/input4mips/>).

421

### 422 **3. Model evaluations**

#### 423 **3.1 Site-level evaluations**

424 We compare the simulated carbon and water fluxes to *in situ* measurements at 201  
425 FLUXNET sites (Figure 2). Among these sites, 95 are tree species with the major PFT



426 of ENF and 106 are non-tree species with the maximum number for shrubland. Most  
427 (71%) of sites are located at the middle latitudes (30°-60°N) of the Northern Hemisphere  
428 (NH), especially in the U.S. and Europe. Compared to the earlier evaluations in  
429 YU2015, we have much more sites in the tropics (22 in this study vs. 5 in YU2015),  
430 Asia (20 in this study vs. 1 in YU2015), and Southern Hemisphere (28 in this study vs.  
431 7 in YU2015) in this study.

432

433 Simulated GPP shows correlation coefficients (R) of 0.59-0.86 for the six main PFTs  
434 with varied sample numbers (Figure 3). The highest R is achieved for ENF, though the  
435 model underestimates the mean GPP magnitude by 20.62% for this species. On average,  
436 simulated GPP is lower than observations for most PFTs. Compared to the YIBs model,  
437 iMAPLE with coupled water cycle improves the GPP simulations for ENF and  
438 grassland but worsens the predictions for other species. The main cause of such deficit  
439 is the application of MERRA-2 reanalyses in the iMAPLE simulations instead of the  
440 site-level meteorology used in the YU2015. The biases in the meteorological input may  
441 cause uncertainties in the simulation of GPP fluxes (Ma et al., 2021). Furthermore, the  
442 increase of site number and record length may decrease the R to some extent.

443

444 Simulated ET matches observations with correlation coefficients of 0.57-0.84 at the  
445 FLUXNET sites (Figure 4). Relatively better performance is achieved for ENF (R=0.83)  
446 and grassland (R=0.84), for which the model yields good predictions of GPP as well.  
447 In contrast, low correlations and high biases are predicted for shrubland and cropland.  
448 For the shrubland sites, different land types (e.g., closed shrublands, permanent  
449 wetlands, and woody savannas) share the same parameters in the iMAPLE model,  
450 resulting in the biases in depicting the site-specific carbon and water fluxes. For  
451 cropland, the prognostic phenology of grass species is applied in the model due to the  
452 missing of plantation information for individual sites. Even with these deficits, the  
453 iMAPLE model in general captures the spatiotemporal variations of GPP and ET at  
454 most sites.



455

456 We further compare the simulated wetland CH<sub>4</sub> fluxes with observations at the  
457 FLUXNET-CH<sub>4</sub> sites. Similar to the carbon flux sites, most of these CH<sub>4</sub> flux sites are  
458 located in the NH (Figure 5a). However, different from the carbon fluxes which usually  
459 range from 0 to 15 g C m<sup>-2</sup> day<sup>-1</sup>, the CH<sub>4</sub> fluxes show a wide range across several  
460 orders of magnitude from 10<sup>-2</sup> to 10<sup>3</sup> g [CH<sub>4</sub>] m<sup>-2</sup> yr<sup>-1</sup> (Figure 5b). Such a large contrast  
461 requires a more realistic configuration of model parameters to distinguish the large  
462 gradient among sites. For example, US-Tw1 and US-Twt are two nearby sites within a  
463 distance of 1 km. However, average CH<sub>4</sub> flux shows a difference of 3.7 times with 66.31  
464 g[CH<sub>4</sub>] m<sup>-2</sup> yr<sup>-1</sup> in US-Tw1 and 18.16 g[CH<sub>4</sub>] m<sup>-2</sup> yr<sup>-1</sup> in US-Tw4 during 2011-2017. In  
465 the model, these two sites share the same land surface properties because they are  
466 located on the same grid. On average, simulated CH<sub>4</sub> fluxes are correlated with  
467 observations at a moderate R of 0.68 and a normalized mean bias (NMB) of -28%.

468

### 469 3.2 Grid-level evaluations

470 The coupling of Noah-MP module enables the dynamic prediction of soil parameters  
471 by the iMAPLE model. We compare the simulated soil moisture and soil temperature  
472 with MERRA-2 reanalyses (Figure 6). Both simulations (Figure 6a) and observations  
473 (Figure 6b) show low soil moisture over arid and semi-arid regions with the minimum  
474 in North Africa. The model also captures the high soil moisture in tropical rainforest.  
475 However, the prediction underestimates soil moisture in boreal regions in NH (Figure  
476 6c). On the global scale, simulated soil moisture matches observations with a high R of  
477 0.86 and a low NMB of -6.9%. These statistical metrics are further improved for the  
478 simulated soil temperature with the R of 0.99 and NMB of 0.5% against observations  
479 (Figure 6f). The simulation reproduces the observed spatial pattern with a uniform  
480 warming bias.

481

482 Driven with the prognostic soil moisture and temperature, the iMAPLE model predicts  
483 reasonable land carbon and water fluxes (Figure 7). Simulated GPP (Figure 7a)



484 reproduces observed patterns (Figure 7b) with high values in the tropical rainforest,  
485 moderate values in the boreal forests, and low values in the arid regions. The predicted  
486 GPP is higher than observations over the tropical rainforest (Figure 7c). However, such  
487 overestimation may instead be an indicator of biases in the ensemble observations,  
488 which are derived from the empirical models instead of direct measurements (Running  
489 et al., 2004; Yuan et al., 2010). Our site-level evaluations show that iMAPLE predicts  
490 reasonable GPP values at the EBF sites (Figure 3). Despite this inconsistency, the model  
491 yields a high R of 0.92 and a small NMB of 1.3% for GPP against observations on the  
492 global scale (Figure 7c). Simulated ET (Figure 7d) matches the observations (Figure 7e)  
493 with high values in the tropical rainforest and secondary high values in the boreal forest.  
494 In general, the prediction is lower than observations except for the eastern U.S. and  
495 eastern China (Figure 7f). On average, the iMAPLE model shows the R of 0.93 and  
496 NMB of -10.4% in the simulation of ET compared to the ensemble of observations.

497

498 We further compare the simulated GPP with or without dynamic water cycle (Figure 8).  
499 Relative to the simulations driven with MERRA-2 soil moisture and temperature, the  
500 iMAPLE model coupled with Noah-MP water module predicts very similar GPP over  
501 the hotspot regions such as tropical rainforest and boreal forest (Figure 8a). However,  
502 the coupled model predicts lower GPP for grassland in the tropics (e.g., South America  
503 and central Africa) but higher GPP in arid regions (e.g., South Africa and Australia).  
504 Since the baseline GPP is very low in arid regions, the relative changes are even larger  
505 than 100% over those areas. These GPP differences are mainly driven by the changes  
506 in soil moisture, which increases over the arid regions with the dynamic water cycle  
507 (Figure 6c). The reduction of soil moisture in the high latitudes of NH shows limited  
508 impacts on the predicted GPP, likely because the boreal ecosystem is more dependent  
509 on temperature than moisture (Beer et al., 2010).

510

### 511 3.3 Ecosystem perturbations to air pollution

512 Within the iMAPLE framework, the land ecosystem perturbs atmospheric components



513 through the emissions from biomass burning, wetland CH<sub>4</sub>, and BVOCs. We compare  
514 the simulated burned fraction with observations from GFED4.1s (Figure 9). The largest  
515 burned fraction is predicted over the Sahel region and countries of Angola and Zambia,  
516 surrounding the low center of Congo rainforest. Moderate burnings could be found in  
517 northern Australia and eastern South America. Most of these hotspots are located on the  
518 grassland and shrubland in the tropics, where the high temperature and limited rainfall  
519 promotes regional fire activities. The model reasonably captures the observed fire  
520 pattern with a spatial correlation of 0.66 and NMB of 6.05% (Figure 9c), though the  
521 model overestimates the area burned in South Africa. The predicted fire area is used to  
522 derive biomass burning emissions of air pollutants (e.g., carbon monoxide, nitrogen  
523 oxides, black carbon, organic carbon, sulfur dioxide) with the specific emission factors  
524 (Tian et al., 2023).

525  
526 The wetland emissions of CH<sub>4</sub> show hotspots over tropical rainforests (Figure 10a),  
527 where the dense soil carbon provides abundant substrates for emissions and the warm  
528 climate promotes the emission rates. The secondary hotspots are located at the boreal  
529 regions in the NH. This spatial pattern is very similar to the map of wetland CH<sub>4</sub>  
530 emissions predicted by an ensemble of 13 biogeochemical models (Saunois et al., 2020).  
531 On the global scale, the total wetland emission is 153.45 Tg [CH<sub>4</sub>] yr<sup>-1</sup> during 2000-  
532 2014, close to the average of 148±25 Tg [CH<sub>4</sub>] yr<sup>-1</sup> for 2000-2017 estimated by the  
533 multiple models. As a comparison, anthropogenic source of CH<sub>4</sub> show the high amount  
534 in China and India due to the large emissions from fossil fuels and agriculture (Figure  
535 10b). On the global scale, the wetland emissions are equivalent to 45.3% of the total  
536 anthropogenic emissions.

537  
538 Isoprene emissions from the two schemes in the iMAPLE model show similar spatial  
539 distributions with the hotspots over tropical rainforest (Figure 11), where the warm  
540 climate and abundant light are favorable for the biogenic emissions. Compared to the  
541 MEGAN scheme, the PS\_BVOC scheme yields higher emissions in the tropical



542 rainforest and boreal forest, but lower emissions for the shrubland and grassland in  
543 semiarid regions (Figure 11c). Such differences are attributed to the varied processes as  
544 well as the emission factors. Our earlier study showed that PS\_BVOC scheme predicts  
545 stronger trends in isoprene emissions than MEGAN (Cao et al., 2021a), because the  
546 former considers both CO<sub>2</sub> fertilization and inhibition effects while the latter considers  
547 only the inhibition effects. On the global scale, isoprene emissions are 550 Tg yr<sup>-1</sup> with  
548 PS\_BVOC (Figure 11a) and 611 Tg yr<sup>-1</sup> with MEGAN (Figure 11b). These amounts are  
549 higher than the ensemble mean of 448 Tg yr<sup>-1</sup> from the CMIP6 models (Cao et al.,  
550 2021b), but in general within the range of 412-601 Tg yr<sup>-1</sup> as summarized by Carslaw  
551 et al. (2010).

552

#### 553 3.4. Air pollution impacts on ecosystem fluxes

554 We assess the damaging effects of surface O<sub>3</sub> to GPP with two schemes (Figure 12).  
555 Simulated GPP losses show similar patterns with high damages in eastern U.S., western  
556 Europe, and eastern China, where surface O<sub>3</sub> level is high due to the anthropogenic  
557 emissions. Limited GPP damages are predicted in the tropics though with abundant  
558 forest coverage due to the low level of O<sub>3</sub> pollution. Compared to the S2007 scheme,  
559 predicted GPP loss is further alleviated in tropical rainforest with the LMA-based  
560 scheme, because the latter scheme determines lower O<sub>3</sub> sensitivity for evergreen trees  
561 due to their higher content of chemical resistance with the larger LMA value (Ma et al.,  
562 2023). On the global scale, the average GPP loss is -2.9% with the LMA scheme and -  
563 3.2% with the S2007 scheme. Such damage to GPP is weaker than the estimate of -4.8%  
564 in Ma et al. (2023) because of the differences in O<sub>3</sub> concentrations, vegetation types,  
565 and photosynthetic parameters.

566

567 Atmospheric aerosols cause perturbations to both direct and diffuse radiation, which  
568 have different efficiencies in enhancing plant photosynthesis. Here, we separate the  
569 diffuse (diffuse fraction > 0.75) and direct (diffuse fraction < 0.25) components of solar  
570 radiation, and aggregate the GPP and ET fluxes for different radiation periods at certain



571 intervals (Figure 13). At the six selected sites, observed GPP is higher and grows faster  
572 with more diffusive light than that under the direct light conditions (Figure 13a-13f).  
573 Simulations in general reproduce such feature with the comparable variability. In the  
574 earlier study, simulated diffuse fertilization efficiency for GPP (changes of GPP per unit  
575 diffuse radiation) was well validated against observations at more than 20 sites (Yue  
576 and Unger, 2018). Such amelioration of GPP suggests that moderate aerosol loading is  
577 beneficial for ecosystem carbon uptake (Yue and Unger, 2017). However, the dense  
578 aerosol loading may instead weaken plant photosynthesis due to the large reduction in  
579 direct radiation .

580

581 We further evaluate the ET responses to diffuse and direct radiation from the iMAPLE  
582 model (Figure 13g-13l). Although ET is slightly higher at the diffusive condition, the  
583 growth rates are weaker than that of GPP. The main cause of such difference is related  
584 to the varied light dependence of ET components, which consist of canopy evaporation  
585 and transpiration. Transpiration is tightly coupled with photosynthesis and will increase  
586 by diffuse radiation at a similar rate. However, evaporation is more dependent on light  
587 quantity which will decrease with the extinction of aerosols. As a result, the weakened  
588 evaporation in part offsets the increased transpiration, leading to the smaller growth rate  
589 of ET than the responses of photosynthesis and the consequent enhancement in water  
590 use efficiency (Wang et al., 2023). The iMAPLE model reasonably captures the lower  
591 growth rates of ET than GPP in response to diffuse radiation at the selected sites.

592

593

#### 594 **4. Conclusions and discussion**

595 We develop the iMAPLE model by coupling Noah-MP water module with YIBs  
596 vegetation model. Validations show that iMAPLE predicts reasonable distribution of  
597 soil moisture and soil temperature. Driven with these prognostic soil conditions and  
598 meteorology from reanalyses, the model reasonably reproduces the observed  
599 spatiotemporal variations of both GPP and ET fluxes at 201 sites and on the global scale.



600 We further update the biogeochemical processes in iMAPLE to extend the model's  
601 capability in quantifying interactions between air pollution and land ecosystems. The  
602 model reasonably predicts wetland CH<sub>4</sub> emissions at 44 sites and yields the similar  
603 global map of CH<sub>4</sub> emissions compared to an ensemble of 13 biogeochemical models.  
604 In addition, predicted biomass burning and biogenic emissions are consistent with  
605 either satellite retrievals or results from other models. We assess the impacts of surface  
606 O<sub>3</sub> and aerosols on ecosystem fluxes. The LMA-based scheme links the O<sub>3</sub> sensitivity  
607 with vegetation LMA and predicts a global map of GPP loss that is consistent with the  
608 traditional scheme using the PFT-specific sensitivity. The updated scheme effectively  
609 reduces modeling uncertainties by decreasing the number of parameters for O<sub>3</sub>  
610 sensitivity and provides an option to apply the advanced LMA map from remote sensing.  
611 The model also reproduces the observed responses of GPP and ET to diffuse radiation  
612 with a lower growth rate for ET than GPP.

613

614 There are several limitations in the current version of iMAPLE model. First, it does not  
615 include the dynamic nutrient cycle. Although we implement the down regulation from  
616 Arora et al. (2009) to constrain CO<sub>2</sub> fertilization, this limitation is dependent only on  
617 the ambient CO<sub>2</sub> concentrations and could not represent the heterogeneous distribution  
618 of nutrients. As a result, the model could not reveal the biogeochemical effects of  
619 nitrogen and phosphorus deposition on land ecosystems. Second, the feedback of fire  
620 activities to ecosystems is ignored. The iMAPLE considers the impacts of fuel load on  
621 area burned at each modeling time step. However, these fire perturbations do not in turn  
622 change the vegetation distribution and composition. The vegetation model does not  
623 consider the competition among PFTs, so that fire perturbations are not allowed to  
624 change vegetation coverage. As a result, the interactions between fire and ecosystems  
625 are underestimated in the current model framework. Third, iMAPLE does not consider  
626 the dynamic changes in wetland area for CH<sub>4</sub> emissions. Although the Noah-MP  
627 module predicts runoff and underground water, the changes of hydrological cycles are  
628 not connected with wetland area in the model. Instead, a prescribed wetland dataset is



629 applied to reduce the possible uncertainties but meanwhile refrain the explorations of  
630 CH<sub>4</sub> changes in the historical and future periods. These limitations will be the focuses  
631 of model development in the next step.

632

633 The iMAPLE model inherits the good capability of the original YIBs model in the  
634 simulations of carbon cycle. Furthermore, the iMAPLE upgrades the YIBs model with  
635 carbon-water coupling and more biogeochemical processes. With the iMAPLE model,  
636 we could assess the changes of carbon and water fluxes, as well as their coupling, in  
637 response to environmental perturbations (e.g., climate change, air pollution, land cover  
638 change). Meanwhile, by coupling the iMAPLE with climate and/or chemical models,  
639 we could further quantify the changes of meteorology and atmospheric components in  
640 response to the biogeochemical and biogeophysical processes. For example, Lei et al.  
641 (2022) revealed the strong vegetation feedback to global surface O<sub>3</sub> during the drought  
642 periods using the YIBs model coupled to a chemical transport model. Xie et al. (2019)  
643 found a significant increase in atmospheric CO<sub>2</sub> concentrations due to O<sub>3</sub>-induced  
644 vegetation damage using the YIBs model coupled with a regional climate-chemistry  
645 model. Gong et al. (2021) estimated a surface warming in polluted regions due to the  
646 ozone-vegetation feedback using the YIBs model coupled with a global climate-  
647 chemistry model. These studies indicate that the iMAPLE model could be used either  
648 offline or online with other models to explore the interactions among climate, chemistry,  
649 and ecosystems.

650

651 *Acknowledgment.* This work was jointly supported by the National Key Research and  
652 Development Program of China (grant no. 2019YFA0606802), the National Natural  
653 Science Foundation of China (grant no. 42275128).

654

655 *Author contributions.* XY, HL designed the research and wrote the paper. XY, HaZ  
656 optimized codes, performed simulations, and analyzed results. XY, HaZ, CT, YM, YH,  
657 CG implemented codes and collected data. HuZ helped with code implementations. All



658 authors commented on and revised the manuscript.

659

660 *Competing interests.* The contact author has declared that none of the authors has any  
661 competing interests.

662

663 *Code availability.* The code for the iMAPLE version 1 model is available at  
664 <https://doi.org/10.6084/m9.figshare.23593578.v1>

665

666 *Data availability.* All the validation data are available to download from the cited  
667 references or data links shown in Section 2.4. The simulation data of monthly output  
668 from BASE experiment during 1980-2021 with the iMAPLE model are available at  
669 <https://doi.org/10.6084/m9.figshare.23593578.v1>

670

## 671 **Reference**

- 672 Arora, V. K., Boer, G. J., Christian, J. R., Curry, C. L., Denman, K. L., Zahariev, K., Flato, G.  
673 M., Scinocca, J. F., Merryfield, W. J., and Lee, W. G.: The Effect of Terrestrial  
674 Photosynthesis Down Regulation on the Twentieth-Century Carbon Budget Simulated  
675 with the CCCma Earth System Model, *J Climate*, 22, 6066-6088, 2009.
- 676 Ball, J. T., Woodrow, I. E., and Berry, J. A.: A model predicting stomatal conductance and its  
677 contribution to the control of photosynthesis under different environmental conditions.  
678 In: *Progress in Photosynthesis Research*, Biggins, J. (Ed.), Nijhoff, Dordrecht, Netherlands,  
679 1987.
- 680 Beer, C., Reichstein, M., Tomelleri, E., Ciais, P., Jung, M., Carvalhais, N., Rodenbeck, C., Arain,  
681 M. A., Baldocchi, D., Bonan, G. B., Bondeau, A., Cescatti, A., Lasslop, G., Lindroth, A.,  
682 Lomas, M., Luyssaert, S., Margolis, H., Oleson, K. W., Rouspard, O., Veenendaal, E.,  
683 Viovy, N., Williams, C., Woodward, F. I., and Papale, D.: Terrestrial Gross Carbon Dioxide  
684 Uptake: Global Distribution and Covariation with Climate, *Science*, 329, 834-838, 2010.
- 685 Cao, Y., Yue, X., Lei, Y., Zhou, H., Liao, H., Song, Y., Bai, J., Yang, Y., Chen, L., Zhu, J., Ma,  
686 Y., and Tian, C.: Identifying the drivers of modeling uncertainties in isoprene emissions:  
687 schemes versus meteorological forcings, *Journal of Geophysical Research*, 126,  
688 e2020JD034242, 2021a.
- 689 Cao, Y., Yue, X., Liao, H., Yang, Y., Zhu, J., Chen, L., Tian, C., Lei, Y., Zhou, H., and Ma, Y.:  
690 Ensemble projection of global isoprene emissions by the end of 21st century using CMIP6  
691 models, *Atmospheric Environment*, 267, 118766, 2021b.
- 692 Carslaw, K. S., Boucher, O., Spracklen, D. V., Mann, G. W., Rae, J. G. L., Woodward, S., and  
693 Kulmala, M.: A review of natural aerosol interactions and feedbacks within the Earth  
694 system, *Atmos Chem Phys*, 10, 1701-1737, 2010.



- 695 Castillo, C. K. G., Levis, S., and Thornton, P.: Evaluation of the New CNDV Option of the  
696 Community Land Model: Effects of Dynamic Vegetation and Interactive Nitrogen on  
697 CLM4 Means and Variability, *J Climate*, 25, 3702-3714, 2012.
- 698 Chen, G., Guo, Y., Yue, X., Tong, S., Gasparrini, A., Bell, M. L., Armstrong, B., Schwartz, J.,  
699 Jouni J K Jaakkola, Zanobetti, A., Lavigne, E., Saldiva, P. H. N., Kan, H., Royé, D.,  
700 Milojevic, A., Overcenco, A., Urban, A., Schneider, A., Entezari, A., Vicedo-Cabrera, A.  
701 M., Zeka, A., Tobias, A., Nunes, B., Alahmad, B., Bertil Forsberg, Pan, S.-C., Íñiguez, C.,  
702 Ameling, C., Valencia, C. D. I. C., Åström, C., Houthuijs, D., Dung, D. V., Samoli, E.,  
703 Mayvaneh, F., Sera, F., Carrasco-Escobar, G., Lei, Y., Orru, H., Kim, H., Iulian-Horia  
704 Holobaca, Kyselý, J., Teixeira, J. P., Madureira, J., Katsouyanni, K., Hurtado-Díaz, M.,  
705 Maasikmets, M., Ragettli, M. S., Hashizume, M., Stafoggia, M., Pascal, M., Scortichini,  
706 M., Micheline de Sousa Zanotti Stagliorio Coêlho, Ortega, N. V., Ryti, N. R. I., Scovronick,  
707 N., Matus, P., Goodman, P., Garland, R. M., Abrutzky, R., Garcia, S. O., Rao, S., Fratianni,  
708 S., Dang, T. N., Colistro, V., Huber, V., Lee, W., Seposo, X., Honda, Y., Guo, Y. L., Ye, T.,  
709 Yu, W., Abramson, M. J., Samet, J. M., and Li, S.: Mortality risk attributable to wildfire-  
710 related PM<sub>2.5</sub> pollution: a global time series study in 749 locations, *The Lancet Planetary*  
711 *Health*, 5, e579-e587, 2021.
- 712 Clapp, R. B. and Hornberger, G. M.: Empirical equations for some soil hydraulic properties,  
713 *Water Resources Research*, 14, 601-604, 1978.
- 714 Cox, P. M.: Description of the "TRIFFID" Dynamic Global Vegetation Model, Hadley Centre  
715 technical note 24, Berks, UK, 2001.
- 716 Defries, R. S., Hansen, M. C., Townshend, J. R. G., Janetos, A. C., and Loveland, T. R.: A new  
717 global 1-km dataset of percentage tree cover derived from remote sensing, *Global Change*  
718 *Biology*, 6, 247-254, 2000.
- 719 Delwiche, K. B. and Knox, S. H. and Malhotra, A. and Fluet-Chouinard, E. and McNicol, G.  
720 and Feron, S. and Ouyang, Z. and Papale, D. and Trotta, C. and Canfora, E. and Cheah, Y.  
721 W. and Christianson, D. and Alberto, M. C. R. and Alekseychik, P. and Aurela, M. and  
722 Baldocchi, D. and Bansal, S. and Billesbach, D. P. and Bohrer, G. and Bracho, R. and  
723 Buchmann, N. and Campbell, D. I. and Celis, G. and Chen, J. and Chen, W. and Chu, H.  
724 and Dalmagro, H. J. and Dengel, S. and Desai, A. R. and Detto, M. and Dolman, H. and  
725 Eichelmann, E. and Euskirchen, E. and Famulari, D. and Fuchs, K. and Goeckede, M. and  
726 Gogo, S. and Gondwe, M. J. and Goodrich, J. P. and Gottschalk, P. and Graham, S. L. and  
727 Heimann, M. and Helbig, M. and Helfter, C. and Hemes, K. S. and Hirano, T. and Hollinger,  
728 D. and Hörtnagl, L. and Iwata, H. and Jacotot, A. and Jurasinski, G. and Kang, M. and  
729 Kasak, K. and King, J. and Klatt, J. and Koebsch, F. and Krauss, K. W. and Lai, D. Y. F.  
730 and Lohila, A. and Mammarella, I. and Beelli Marchesini, L. and Manca, G. and Matthes,  
731 J. H. and Maximov, T. and Merbold, L. and Mitra, B. and Morin, T. H. and Nemitz, E. and  
732 Nilsson, M. B. and Niu, S. and Oechel, W. C. and Oikawa, P. Y. and Ono, K. and Peichl,  
733 M. and Peltola, O. and Reba, M. L. and Richardson, A. D. and Riley, W. and Runkle, B. R.  
734 K. and Ryu, Y. and Sachs, T. and Sakabe, A. and Sanchez, C. R. and Schuur, E. A. and  
735 Schäfer, K. V. R. and Sonntag, O. and Sparks, J. P. and Stuart-Haëntjens, E. and  
736 Sturtevant, C. and Sullivan, R. C. and Szutu, D. J. and Thom, J. E. and Torn, M. S. and  
737 Tuittila, E. S. and Turner, J. and Ueyama, M. and Valach, A. C. and Vargas, R. and Varlagin,  
738 A. and Vazquez-Lule, A. and Verfaillie, J. G. and Vesala, T. and Vourlitis, G. L. and Ward,



- 739 E. J. and Wille, C. and Wohlfahrt, G. and Wong, G. X. and Zhang, Z. and Zona, D. and  
740 Windham-Myers, L. and Poulter, B. and Jackson, R. B.: FLUXNET-CH4: a global, multi-  
741 ecosystem dataset and analysis of methane seasonality from freshwater wetlands, *Earth*  
742 *Syst. Sci. Data*, 13, 3607-3689, 2021.
- 743 Farquhar, G. D., Caemmerer, S. V., and Berry, J. A.: A Biochemical-Model of Photosynthetic  
744 Co2 Assimilation in Leaves of C-3 Species, *Planta*, 149, 78-90, 1980.
- 745 Friedlingstein, P. and O'Sullivan, M. and Jones, M. W. and Andrew, R. M. and Gregor, L. and  
746 Hauck, J. and Quéré, C. L. and Luijkx, I. T. and Olsen, A. and Peters, G. P. and Peters, W.  
747 and Pongratz, J. and Schwingshackl, C. and Sitch, S. and Canadell, J. G. and Ciais, P. and  
748 Jackson, R. B. and Alin, S. R. and Alkama, R. and Arneeth, A. and Arora, V. K. and Bates,  
749 N. R. and Becker, M. and Bellouin, N. and Bittig, H. C. and Bopp, L. and Chevallier, F.  
750 and Chini, L. P. and Cronin, M. and Decharme, B. and Evans, W. and Falk, S. and Feely,  
751 R. A. and Gasser, T. and Gehlen, M. and Gkritzalis, T. and Gloege, L. and Grassi, G. and  
752 Gruber, N. and Gürses, Ö. and Harris, I. and Hefner, M. and Houghton, R. A. and Hurtt,  
753 G. C. and Iida, Y. and Ilyina, T. and Jain, A. K. and Jersild, A. and Kadono, K. and Kato,  
754 E. and Kennedy, D. and Goldewijk, K. K. and Knauer, J. and Korsbakken, J. I. and  
755 Landschützer, P. and Lefèvre, N. and Lindsay, K. and Liu, Z. and Liu, J. and Marland, G.  
756 and Mayot, N. and McGrath, M. J. and Metzl, N. and Monacci, N. M. and Munro, D. R.  
757 and Nakaoka, S.-I. and Niwa, Y. and O'Brien, K. and Ono, T. and Palmer, P. I. and Pan, N.  
758 and Pierrot, D. and Pocock, K. and Poulter, B. and Resplandy, L. and Robertson, E. and  
759 Rödenbeck, C. and Rodriguez, C. and Rosan, T. M. and Schwinger, J. and Séférian, R. and  
760 Shutler, J. D. and Skjelvan, I. and Steinhoff, T. and Sun, Q. and Sutton, A. J. and Sweeney,  
761 C. and Takao, S. and Tanhua, T. and Tans, P. P. and Tian, X. and Tian, H. and Tilbrook, B.  
762 and Tsujino, H. and Tubiello, F. and Werf, G. v. d. and Walker, A. P. and Wanninkhof, R.  
763 and Whitehead, C. and Wranne, A. W. and Wright, R. and Yuan, W. and Yue, C. and Yue,  
764 X. and Zaehle, S. and Zeng, J. and Zheng, B.: Global Carbon Budget 2022, *Earth System*  
765 *Science Data*, 14, 4811-4900, 2022.
- 766 Friedlingstein, P., O'Sullivan, M., Jones, M. W., Andrew, R. M., Hauck, J., Olsen, A., Peters, G.  
767 P., Peters, W., Pongratz, J., Sitch, S., Quéré, C. L., Canadell, J. G., Ciais, P. P., Jackson, R.  
768 B., Alin, S., Aragao, L. E., Arneeth, A., Arora, V., Bates, N. R., Becker, M., Benoit-Cattin,  
769 A., Bittig, H. C., Bopp, L., Bultan, S., Chandra, N., Chevallier, F., Chini, L. P., Evans, W.,  
770 Florentie, L., Forster, P. M., Gasser, T., Gehlen, M., Gilfillan, D., Gkritzalis, T., Gregor, L.,  
771 Gruber, N., Harris, I., Hartung, K., Haverd, V., Houghton, R. A., Ilyina, T., Jain, A. K.,  
772 Joetzjer, E., Kadono, K., Kato, E., Kitidis, V., Ivar, J. I. J., Landschützer, P., Lefèvre, N.,  
773 Lenton, A., Lienert, S., Liu, Z., Lombardozi, D., Marland, G., Metzl, N., Munro, D. R.,  
774 Nabel, J. E., Nakaoka, S.-I., Niwa, Y., O'Brien, K., Ono, T., Palmer, P. I., Pierrot, D.,  
775 Poulter, B., Resplandy, L., Robertson, E., Rödenbeck, C., Schwinger, J., Séférian, R.,  
776 Skjelvan, I., Smith, A. J., Sutton, A., Tanhua, T., Tans, P. P., Tian, H., Tilbrook, B., Werf,  
777 G. R. v. d., Vuichard, N., Walker, A., Wanninkhof, R., Watson, A. J., Willis, D., Wiltshire,  
778 A. J., Yuan, W., Yue, X., and Zaehle, S.: Global Carbon Budget 2020, *Earth System Science*  
779 *Data*, 12, 3269-3340, 2020.
- 780 Gelaro, R., McCarty, W., Suarez, M. J., Todling, R., Molod, A., Takacs, L., Randles, C. A.,  
781 Darnenov, A., Bosilovich, M. G., Reichle, R., Wargan, K., Coy, L., Cullather, R., Draper,  
782 C., Akella, S., Buchard, V., Conaty, A., da Silva, A. M., Gu, W., Kim, G. K., Koster, R.,



- 783 Lucchesi, R., Merkova, D., Nielsen, J. E., Partyka, G., Pawson, S., Putman, W., Rienecker,  
784 M., Schubert, S. D., Sienkiewicz, M., and Zhao, B.: The Modern-Era Retrospective  
785 Analysis for Research and Applications, Version 2 (MERRA-2), *J Climate*, 30, 5419-5454,  
786 2017.
- 787 Gong, C., Liao, H., Yue, X., Ma, Y., and Lei, Y.: Impacts of ozone-vegetation interactions on  
788 ozone pollution episodes in North China and the Yangtze River Delta, *Geophys Res Lett*,  
789 48, e2021GL093814, 2021.
- 790 Guenther, A. B., Jiang, X., Heald, C. L., Sakulyanontvittaya, T., Duhl, T., Emmons, L. K., and  
791 Wang, X.: The Model of Emissions of Gases and Aerosols from Nature version 2.1  
792 (MEGAN2.1): an extended and updated framework for modeling biogenic emissions,  
793 *Geosci Model Dev*, 5, 1471-1492, 2012.
- 794 Hansen, M. C., DeFries, R. S., Townshend, J. R. G., Carroll, M., Dimiceli, C., and Sohlberg, R.  
795 A.: Global Percent Tree Cover at a Spatial Resolution of 500 Meters: First Results of the  
796 MODIS Vegetation Continuous Fields Algorithm, *Earth Interact*, 7, 1-15, 2003.
- 797 Heimann, I., Griffiths, P. T., Warwick, N. J., Abraham, N. L., Archibald, A. T., and Pyle, J. A.:  
798 Methane Emissions in a Chemistry-Climate Model: Feedbacks and Climate Response, *J*  
799 *Adv Model Earth Sy*, 12, e2019MS002019, 2020.
- 800 Hengl, T., de Jesus, J. M., Heuvelink, G. B. M., Gonzalez, M. R., Kilibarda, M., Blagotic, A.,  
801 Shangguan, W., Wright, M. N., Geng, X. Y., Bauer-Marschallinger, B., Guevara, M. A.,  
802 Vargas, R., MacMillan, R. A., Batjes, N. H., Leenaars, J. G. B., Ribeiro, E., Wheeler, I.,  
803 Mantel, S., and Kempen, B.: SoilGrids250m: Global gridded soil information based on  
804 machine learning, *Plos One*, 12, 2017.
- 805 Jasechko, S., Sharp, Z. D., Gibson, J. J., Birks, S. J., Yi, Y., and Fawcett, P. J.: Terrestrial water  
806 fluxes dominated by transpiration, *Nature*, 496, 347-350, 2013.
- 807 Jung, M., Reichstein, M., Margolis, H. A., Cescatti, A., Richardson, A. D., Arain, M. A., Arneth,  
808 A., Bernhofer, C., Bonal, D., Chen, J. Q., Gianelle, D., Gobron, N., Kiely, G., Kutsch, W.,  
809 Lasslop, G., Law, B. E., Lindroth, A., Merbold, L., Montagnani, L., Moors, E. J., Papale,  
810 D., Sottocornola, M., Vaccari, F., and Williams, C.: Global patterns of land-atmosphere  
811 fluxes of carbon dioxide, latent heat, and sensible heat derived from eddy covariance,  
812 satellite, and meteorological observations, *Journal of Geophysical Research*, 116, G00j07,  
813 2011.
- 814 Jung, M., Schwalm, C., Migliavacca, M., Walther, S., Camps-Valls, G., Koirala, S., Anthoni, P.,  
815 Besnard, S., Bodesheim, P., Carvalhais, N., Chevallier, F., Gans, F., Goll, D. S., Haverd,  
816 V., Köhler, P., Ichii, K., Jain, A. K., Liu, J., Lombardozi, D., Nabel, J. E. M. S., Nelson,  
817 J. A., O'Sullivan, M., Pallandt, M., Papale, D., Peters, W., Pongratz, J., Rödenbeck, C.,  
818 Sitch, S., Tramontana, G., Walker, A., Weber, U., and Reichstein, M.: Scaling carbon fluxes  
819 from eddy covariance sites to globe: synthesis and evaluation of the FLUXCOM approach,  
820 *Biogeosciences*, 17, 1343-1365, 2020a.
- 821 Jung, M., Schwalm, C., Migliavacca, M., Walther, S., Camps-Valls, G., Koirala, S., Anthoni, P.,  
822 Besnard, S., Bodesheim, P., Carvalhais, N., Chevallier, F., Gans, F., Goll, D. S., Haverd,  
823 V., Kohler, P., Ichii, K., Jain, A. K., Liu, J. Z., Lombardozi, D., Nabel, J. E. M. S., Nelson,  
824 J. A., O'Sullivan, M., Pallandt, M., Papale, D., Peters, W., Pongratz, J., Rodenbeck, C.,  
825 Sitch, S., Tramontana, G., Walker, A., Weber, U., and Reichstein, M.: Scaling carbon fluxes  
826 from eddy covariance sites to globe: synthesis and evaluation of the FLUXCOM approach,



- 827 Biogeosciences, 17, 1343-1365, 2020b.
- 828 Kattge, J. and Diaz, S. and Lavorel, S. and Prentice, C. and Leadley, P. and Bonisch, G. and  
829 Garnier, E. and Westoby, M. and Reich, P. B. and Wright, I. J. and Cornelissen, J. H. C.  
830 and Violle, C. and Harrison, S. P. and van Bodegom, P. M. and Reichstein, M. and Enquist,  
831 B. J. and Soudzilovskaia, N. A. and Ackerly, D. D. and Anand, M. and Atkin, O. and Bahn,  
832 M. and Baker, T. R. and Baldocchi, D. and Bekker, R. and Blanco, C. C. and Blonder, B.  
833 and Bond, W. J. and Bradstock, R. and Bunker, D. E. and Casanoves, F. and Cavender-  
834 Bares, J. and Chambers, J. Q. and Chapin, F. S. and Chave, J. and Coomes, D. and  
835 Cornwell, W. K. and Craine, J. M. and Dobrin, B. H. and Duarte, L. and Durka, W. and  
836 Elser, J. and Esser, G. and Estiarte, M. and Fagan, W. F. and Fang, J. and Fernandez-  
837 Mendez, F. and Fidelis, A. and Finegan, B. and Flores, O. and Ford, H. and Frank, D. and  
838 Freschet, G. T. and Fyllas, N. M. and Gallagher, R. V. and Green, W. A. and Gutierrez, A.  
839 G. and Hickler, T. and Higgins, S. I. and Hodgson, J. G. and Jalili, A. and Jansen, S. and  
840 Joly, C. A. and Kerkhoff, A. J. and Kirkup, D. and Kitajima, K. and Kleyer, M. and Klotz,  
841 S. and Knops, J. M. H. and Kramer, K. and Kuhn, I. and Kurokawa, H. and Laughlin, D.  
842 and Lee, T. D. and Leishman, M. and Lens, F. and Lenz, T. and Lewis, S. L. and Lloyd, J.  
843 and Llusia, J. and Louault, F. and Ma, S. and Mahecha, M. D. and Manning, P. and Massad,  
844 T. and Medlyn, B. E. and Messier, J. and Moles, A. T. and Muller, S. C. and Nadrowski,  
845 K. and Naeem, S. and Niinemets, U. and Nollert, S. and Nuske, A. and Ogaya, R. and  
846 Oleksyn, J. and Onipchenko, V. G. and Onoda, Y. and Ordonez, J. and Overbeck, G. and  
847 Ozinga, W. A. and Patino, S. and Paula, S. and Pausas, J. G. and Penuelas, J. and Phillips,  
848 O. L. and Pillar, V. and Poorter, H. and Poorter, L. and Poschlod, P. and Prinzing, A. and  
849 Proulx, R. and Rammig, A. and Reinsch, S. and Reu, B. and Sack, L. and Salgado-Negre,  
850 B. and Sardans, J. and Shiodera, S. and Shipley, B. and Siefert, A. and Sosinski, E. and  
851 Soussana, J. F. and Swaine, E. and Swenson, N. and Thompson, K. and Thornton, P. and  
852 Waldram, M. and Weiher, E. and White, M. and White, S. and Wright, S. J. and Yguel, B.  
853 and Zaehle, S. and Zanne, A. E. and Wirth, C.: TRY - a global database of plant traits,  
854 *Global Change Biology*, 17, 2905-2935, 2011.
- 855 Keeling, C. D., Bacastow, R. B., Bainbridge, A. E., Ekdahl, C. A., Guenther, P. R., Waterman,  
856 L. S., and Chin, J. F. S.: Atmospheric carbon dioxide variations at Mauna Loa Observatory,  
857 Hawaii, *Tellus A.*, 28, 538-551, 1976.
- 858 Lei, Y., Yue, X., Liao, H., Gong, C., and Zhang, L.: Implementation of Yale Interactive  
859 terrestrial Biosphere model v1.0 into GEOS-Chem v12.0.0: a tool for biosphere-chemistry  
860 interactions, *Geosci Model Dev*, 13, 1137-1153, 2020.
- 861 Lei, Y., Yue, X., Liao, H., Zhang, L., Zhou, H., Tian, C., Gong, C., Ma, Y., Cao, Y., Seco, R.,  
862 Karl, T., and Potosnak, M.: Global perspective of drought impacts on ozone pollution  
863 episodes, *Environmental Science & Technology*, 56, 3932-3940, 2022.
- 864 Li, F., Zeng, X. D., and Levis, S.: A process-based fire parameterization of intermediate  
865 complexity in a Dynamic Global Vegetation Model (vol 9, pg 2761, 2012), *Biogeosciences*,  
866 9, 4771-4772, 2012.
- 867 Li, X. and Xiao, J.: Mapping Photosynthesis Solely from Solar-Induced Chlorophyll  
868 Fluorescence: A Global, Fine-Resolution Dataset of Gross Primary Production Derived  
869 from OCO-2, *Remote Sensing*, 11, 2563, 2019.
- 870 Lin, M. Y., Horowitz, L. W., Xie, Y. Y., Paulot, F., Malyshev, S., Shevliakova, E., Finco, A.,



- 871 Gerosa, G., Kubistin, D., and Pilegaard, K.: Vegetation feedbacks during drought  
872 exacerbate ozone air pollution extremes in Europe, *Nat Clim Change*, 10, 444-451, 2020.
- 873 Lombardozi, D., Levis, S., Bonan, G., Hess, P. G., and Sparks, J. P.: The Influence of Chronic  
874 Ozone Exposure on Global Carbon and Water Cycles, *J Climate*, 28, 292-305, 2015.
- 875 Ma, Y., Yue, X., Sitch, S., Unger, N., Uddling, J., Mercado, L. M., Gong, C., Feng, Z., Yang,  
876 H., Zhou, H., Tian, C., Cao, Y., Lei, Y., Cheesman, A. W., Xu, Y., and Rojas, M. C. D.:  
877 Implementation of trait-based ozone plant sensitivity in the Yale Interactive terrestrial  
878 Biosphere model v1.0 to assess global vegetation damage, *Geosci Model Dev*, 16, 2261-  
879 2276, 2023.
- 880 Ma, Y., Yue, X., Zhou, H., Gong, C., Lei, Y., Tian, C., and Cao, Y.: Identifying the dominant  
881 climate-driven uncertainties in modeling gross primary productivity, *Science of the Total  
882 Environment*, 800, 149518, 2021.
- 883 Madani, N., Kimball, J. S., and Running, S. W.: Improving Global Gross Primary Productivity  
884 Estimates by Computing Optimum Light Use Efficiencies Using Flux Tower Data, *Journal  
885 of Geophysical Research-Biogeosciences*, 122, 2939-2951, 2017.
- 886 Mercado, L. M., Bellouin, N., Sitch, S., Boucher, O., Huntingford, C., Wild, M., and Cox, P.  
887 M.: Impact of changes in diffuse radiation on the global land carbon sink, *Nature*, 458,  
888 1014-U1087, 2009.
- 889 Moreno-Martínez, Á., Camps-Valls, G., Kattge, J., Robinson, N., Reichstein, M., Bodegom, P.  
890 V., and Running, S. W.: Global maps of leaf traits at 3km resolution, TRY File Archive.  
891 2018.
- 892 Niu, G. Y., Yang, Z. L., Mitchell, K. E., Chen, F., Ek, M. B., Barlage, M., Kumar, A., Manning,  
893 K., Niyogi, D., Rosero, E., Tewari, M., and Xia, Y. L.: The community Noah land surface  
894 model with multiparameterization options (Noah-MP): 1. Model description and  
895 evaluation with local-scale measurements, *Journal of Geophysical Research*, 116, D12109,  
896 2011.
- 897 Paudel, R., Mahowald, N. M., Hess, P. G. M., Meng, L., and Riley, W. J.: Attribution of changes  
898 in global wetland methane emissions from pre-industrial to present using CLM4.5-BGC,  
899 *Environ Res Lett*, 11, 034020, 2016.
- 900 Pechony, O. and Shindell, D. T.: Fire parameterization on a global scale, *Journal of Geophysical  
901 Research-Atmospheres*, 114, D16115, 2009.
- 902 Piao, S. L., Ciais, P., Friedlingstein, P., de Noblet-Ducoudre, N., Cadule, P., Viovy, N., and  
903 Wang, T.: Spatiotemporal patterns of terrestrial carbon cycle during the 20th century,  
904 *Global Biogeochem Cy*, 23, Gb4026, 2009.
- 905 Randerson, J. T., Chen, Y., van der Werf, G. R., Rogers, B. M., and Morton, D. C.: Global  
906 burned area and biomass burning emissions from small fires, *Journal of Geophysical  
907 Research-Biogeosciences*, 117, G04012, 2012.
- 908 Rap, A., Scott, C. E., Reddington, C. L., Mercado, L., Ellis, R. J., Garraway, S., Evans, M. J.,  
909 Beerling, D. J., MacKenzie, A. R., Hewitt, C. N., and Spracklen, D. V.: Enhanced global  
910 primary production by biogenic aerosol via diffuse radiation fertilization, *Nat Geosci*, 11,  
911 640-644, 2018.
- 912 Rosentreter, J. A., Borges, A. V., Deemer, B. R., Holgerson, M. A., Liu, S. D., Song, C. L.,  
913 Melack, J., Raymond, P. A., Duarte, C. M., Allen, G. H., Olefeldt, D., Poulter, B., Battin,  
914 T. I., and Eyre, B. D.: Half of global methane emissions come from highly variable aquatic



- 915 ecosystem sources, *Nature Geoscience*, 14, 225-+, 2021.
- 916 Running, S., Nemani, R., Heinsch, F., Zhao, M., Reeves, M., and Hashimoto, H.: A continuous  
917 satellite-derived measure of global terrestrial primary production, *BioScience*, 54, 547-  
918 560, 2004.
- 919 Saunois, M., Stavert, A. R., Poulter, B., Bousquet, P., Canadell, J. G., Jackson, R. B., Raymond,  
920 P. A., Dlugokencky, E. J., Houweling, S., Patra, P. K., Ciais, P., Arora, V. K., Bastviken,  
921 D., Bergamaschi, P., Blake, D. R., Brailsford, G., Bruhwiler, L., Carlson, K. M., Carrol,  
922 M., Castaldi, S., Chandra, N., Crevoisier, C., Crill, P. M., Covey, K., Curry, C. L., Etiope,  
923 G., Frankenberg, C., Gedney, N., Hegglin, M. I., Hoglund-Isaksson, L., Hugelius, G.,  
924 Ishizawa, M., Ito, A., Janssens-Maenhout, G., Jensen, K. M., Joos, F., Kleinen, T.,  
925 Krummel, P. B., Langenfelds, R. L., Laruelle, G. G., Liu, L. C., Machida, T., Maksyutov,  
926 S., McDonald, K. C., McNorton, J., Miller, P. A., Melton, J. R., Morino, I., Muller, J.,  
927 Murguia-Flores, F., Naik, V., Niwa, Y., Noce, S., Doherty, S. O., Parker, R. J., Peng, C. H.,  
928 Peng, S. S., Peters, G. P., Prigent, C., Prinn, R., Ramonet, M., Regnier, P., Riley, W. J.,  
929 Rosentreter, J. A., Segers, A., Simpson, I. J., Shi, H., Smith, S. J., Steele, L. P., Thornton,  
930 B. F., Tian, H. Q., Tohjima, Y., Tubiello, F. N., Tsuruta, A., Viovy, N., Voulgarakis, A.,  
931 Weber, T. S., van Weele, M., van der Werf, G. R., Weiss, R. F., Worthy, D., Wunch, D., Yin,  
932 Y., Yoshida, Y., Zhang, W. X., Zhang, Z., Zhao, Y. H., Zheng, B., Zhu, Q., Zhu, Q. A., and  
933 Zhuang, Q. L.: The Global Methane Budget 2000-2017, *Earth System Science Data*, 12,  
934 1561-1623, 2020.
- 935 Schaake, J. C., Koren, V. I., Duan, Q.-Y., Mitchell, K., and Chen, F.: Simple water balance  
936 model for estimating runoff at different spatial and temporal scales, *Journal of Geophysical*  
937 *Research*, 101, 7461-7475, 1996.
- 938 Schaefer, K., Collatz, G. J., Tans, P., Denning, A. S., Baker, I., Berry, J., Prihodko, L., Suits, N.,  
939 and Philpott, A.: Combined Simple Biosphere/Carnegie-Ames-Stanford Approach  
940 terrestrial carbon cycle model, *J Geophys Res-Bioge*, 113, G03034, 2008.
- 941 Scholes, R. J., Colstoun, E. B. d., Hall, F. G., Collatz, G. J., Meeson, B. W., Los, S. O., and  
942 Landis, D. R.: ISLSCP II Global Gridded Soil Characteristics. ORNL DAAC, Oak Ridge,  
943 Tennessee, USA, 2011.
- 944 Sitch, S., Cox, P. M., Collins, W. J., and Huntingford, C.: Indirect radiative forcing of climate  
945 change through ozone effects on the land-carbon sink, *Nature*, 448, 791-794, 2007.
- 946 Sitch, S., Friedlingstein, P., Gruber, N., Jones, S. D., Murray-Tortarolo, G., Ahlström, A., Doney,  
947 S. C., Graven, H., Heinze, C., Huntingford, C., Levis, S., Levy, P. E., Lomas, M., Poulter,  
948 B., Viovy, N., Zaehle, S., Zeng, N., Arneth, A., Bonan, G., Bopp, L., Canadell, J. G.,  
949 Chevallier, F., Ciais, P., Ellis, R., Gloor, M., Peylin, P., Piao, S. L., Quéré, C. L., Smith, B.,  
950 Zhu, Z., and Myneni, R.: Recent trends and drivers of regional sources and sinks of carbon  
951 dioxide, *Biogeosciences*, 12, 653-679, 2015.
- 952 Spitters, C. J. T.: Separating the Diffuse and Direct Component of Global Radiation and Its  
953 Implications for Modeling Canopy Photosynthesis .2. Calculation of Canopy  
954 Photosynthesis, *Agr Forest Meteorol*, 38, 231-242, 1986.
- 955 Spracklen, D. V., Arnold, S. R., and Taylor, C. M.: Observations of increased tropical rainfall  
956 preceded by air passage over forests, *Nature*, 489, 282-U127, 2012.
- 957 Terrer, C., Jackson, R. B., Prentice, I. C., Keenan, T. F., Kaiser, C., Vicca, S., Fisher, J. B., Reich,  
958 P. B., Stocker, B. D., Hungate, B. A., Penuelas, J., McCallum, I., Soudzilovskaia, N. A.,



- 959 Cernusak, L. A., Talhelm, A. F., Van Sundert, K., Piao, S. L., Newton, P. C. D., Hovenden,  
960 M. J., Blumenthal, D. M., Liu, Y. Y., Muller, C., Winter, K., Field, C. B., Viechtbauer, W.,  
961 Van Lissa, C. J., Hoosbeek, M. R., Watanabe, M., Koike, T., Leshyk, V. O., Polley, H. W.,  
962 and Franklin, O.: Nitrogen and phosphorus constrain the CO<sub>2</sub> fertilization of global plant  
963 biomass, *Nat Clim Change*, 9, 684-689, 2019.
- 964 Tian, C., Yue, X., Zhu, J., Liao, H., Yang, Y., Chen, L., Zhou, X., Lei, Y., Zhou, H., and Cao, Y.:  
965 Projections of fire emissions and the consequent impacts on air quality under 1.5°C and  
966 2°C global warming, *Environmental Pollution*, 323, 121311, 2023.
- 967 Tian, C., Yue, X., Zhu, J., Liao, H., Yang, Y., Lei, Y., Zhou, X., Zhou, H., Ma, Y., and Cao, Y.:  
968 Fire-climate interactions through aerosol radiative effect in a global chemistry-climate-  
969 vegetation model, *Atmos Chem Phys*, 22, 12353-12366, 2022.
- 970 Unger, N., Harper, K., Zheng, Y., Kiang, N. Y., Aleinov, I., Arneth, A., Schurgers, G., Amelynck,  
971 C., Goldstein, A., Guenther, A., Heinesch, B., Hewitt, C. N., Karl, T., Laffineur, Q.,  
972 Langford, B., McKinney, K. A., Misztal, P., Potosnak, M., Rinne, J., Pressley, S., Schoon,  
973 N., and Serça, D.: Photosynthesis-dependent isoprene emission from leaf to planet in a  
974 global carbon–chemistry–climate model, *Atmos. Chem. Phys.*, 13, 10243-10269, 2013.
- 975 van der Werf, G. R., Randerson, J. T., Giglio, L., Collatz, G. J., Mu, M., Kasibhatla, P. S.,  
976 Morton, D. C., DeFries, R. S., Jin, Y., and van Leeuwen, T. T.: Global fire emissions and  
977 the contribution of deforestation, savanna, forest, agricultural, and peat fires (1997-2009),  
978 *Atmos Chem Phys*, 10, 11707-11735, 2010.
- 979 Walter, B. P. and Heimann, M.: A process-based, climate-sensitive model to derive methane  
980 emissions from natural wetlands: Application to five wetland sites, sensitivity to model  
981 parameters, and climate, *Global Biogeochem Cy*, 14, 745-765, 2000.
- 982 Walter, B. P., Heimann, M., and Matthews, E.: Modeling modern methane emissions from  
983 natural wetlands: 1. Model description and results, *Journal of Geophysical Research*, 106,  
984 34189-34206, 2001.
- 985 Wang, B., Yue, X., Zhou, H., Lu, X., and Zhu, J.: Enhanced ecosystem water-use efficiency  
986 under the more diffuse radiation conditions, *Global Biogeochem Cy*, 37, e2022GB007606,  
987 2023.
- 988 Wang, S. H., Zhang, Y. G., Ju, W. M., Chen, J. M., Ciais, P., Cescatti, A., Sardans, J., Janssens,  
989 I. A., Wu, M. S., Berry, J. A., Campbell, E., Fernandez-Martinez, M., Alkama, R., Sftch,  
990 S., Friedlingstein, P., Smith, W. K., Yuan, W. P., He, W., Lombardozzi, D., Kautz, M., Zhu,  
991 D., Lienert, S., Kato, E., Poulter, B., Sanders, T. G. M., Kruger, I., Wang, R., Zeng, N.,  
992 Tian, H. Q., Vuichard, N., Jain, A. K., Wiltshire, A., Haverd, V., Goll, D. S., and Penuelas,  
993 J.: Recent global decline of CO<sub>2</sub> fertilization effects on vegetation photosynthesis, *Science*,  
994 370, 1295-1300, 2020.
- 995 Wania, R., Ross, I., and Prentice, I. C.: Implementation and evaluation of a new methane model  
996 within a dynamic global vegetation model: LPJ-WHYMe v1.3.1, *Geosci Model Dev*, 3,  
997 565-584, 2010.
- 998 Warneke, C., Schwarz, J. P., Dibb, J., Kalashnikova, O., Frost, G., Al-Saad, J., Brown, S. S.,  
999 Brewer, W. A., Soja, A., Seidel, F. C., Washenfelder, R. A., Wiggins, E. B., Moore, R. H.,  
1000 Anderson, B. E., Jordan, C., Yacovitch, T. I., Herndon, S. C., Liu, S., Kuwayama, T., Jaffe,  
1001 D., Johnston, N., Selimovic, V., Yokelson, R., Giles, D. M., Holben, B. N., Goloub, P.,  
1002 Popovici, I., Trainer, M., Kumar, A., Pierce, R. B., Fahey, D., Roberts, J., Gargulinski, E.



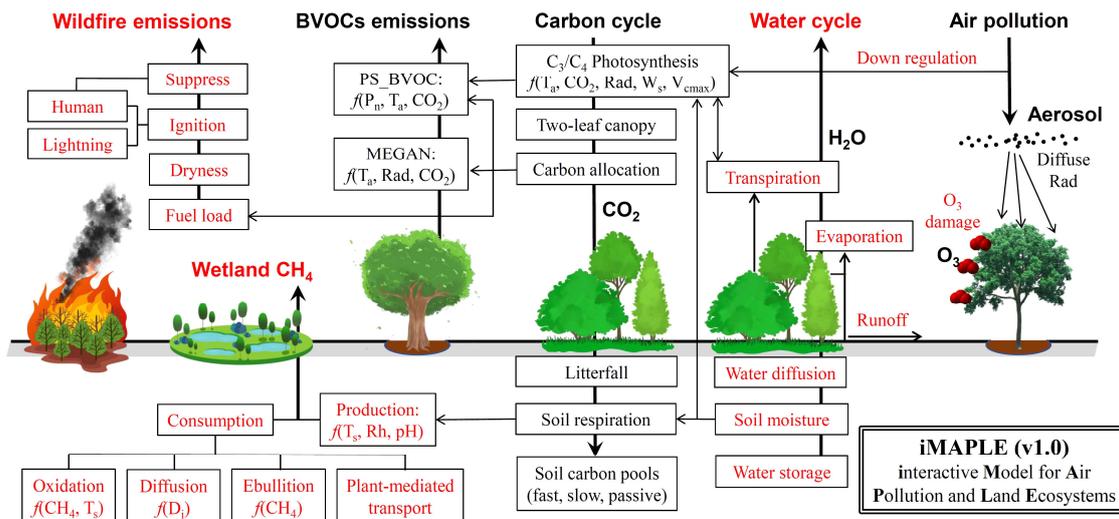
- 1003 M., Peterson, D. A., Ye, X. X., Thapa, L. H., Saide, P. E., Fite, C. H., Holmes, C. D., Wang,  
1004 S. Y., Coggon, M. M., Decker, Z. C. J., Stockwell, C. E., Xu, L., Gkatzelis, G., Aikin, K.,  
1005 Lefer, B., Kaspari, J., Griffin, D., Zeng, L. H., Weber, R., Hastings, M., Chai, J. J., Wolfe,  
1006 G. M., Hanisco, T. F., Liao, J., Jost, P. C., Guo, H. Y., Jimenez, J. L., Crawford, J., and  
1007 Team, F.-A. S.: Fire Influence on Regional to Global Environments and Air Quality  
1008 (FIREX-AQ), *Journal of Geophysical Research*, 128, e2022JD037758, 2023.
- 1009 Worden, J., Saatchi, S., Keller, M., Bloom, A. A., Liu, J., Parazoo, N., Fisher, J. B., Bowman,  
1010 K., Reager, J. T., Fahy, K., Schimel, D., Fu, R., Worden, S., Yin, Y., Gentine, P., Konings,  
1011 A. G., Quetin, G. R., Williams, M., Worden, H., Shi, M. J., and Barkhordarian, A.: Satellite  
1012 Observations of the Tropical Terrestrial Carbon Balance and Interactions With the Water  
1013 Cycle During the 21st Century, *Rev Geophys*, 59, e2020RG000711, 2021.
- 1014 Wu, K., Yang, X. Y., Chen, D., Gu, S., Lu, Y. Q., Jiang, Q., Wang, K., Ou, Y. H., Qian, Y., Shao,  
1015 P., and Lu, S. H.: Estimation of biogenic VOC emissions and their corresponding impact  
1016 on ozone and secondary organic aerosol formation in China, *Atmos Res*, 231, 104656,  
1017 2020.
- 1018 Xie, X., Wang, T., Yue, X., Li, S., Zhuang, B., Wang, M., and Yang, X.: Numerical modeling of  
1019 ozone damage to plants and its effects on atmospheric CO<sub>2</sub> in China, *Atmospheric  
1020 Environment*, 217, 116970, 2019.
- 1021 Yuan, W. P., Liu, S. G., Yu, G. R., Bonnefond, J. M., Chen, J. Q., Davis, K., Desai, A. R.,  
1022 Goldstein, A. H., Gianelle, D., Rossi, F., Suyker, A. E., and Verma, S. B.: Global estimates  
1023 of evapotranspiration and gross primary production based on MODIS and global  
1024 meteorology data, *Remote Sensing of Environment*, 114, 1416-1431, 2010.
- 1025 Yuan, X. Y., Calatayud, V., Gao, F., Fares, S., Paoletti, E., Tian, Y., and Feng, Z. Z.: Interaction  
1026 of drought and ozone exposure on isoprene emission from extensively cultivated poplar,  
1027 *Plant Cell Environ*, 39, 2276-2287, 2016.
- 1028 Yue, X., Keenan, T. F., Munger, W., and Unger, N.: Limited effect of ozone reductions on the  
1029 20-year photosynthesis trend at Harvard forest, *Global Change Biology*, 22, 3750-3759,  
1030 2016.
- 1031 Yue, X. and Unger, N.: Aerosol optical depth thresholds as a tool to assess diffuse radiation  
1032 fertilization of the land carbon uptake in China, *Atmos Chem Phys*, 17, 1329-1342, 2017.
- 1033 Yue, X. and Unger, N.: Fire air pollution reduces global terrestrial productivity, *Nature  
1034 Communications*, 9, 5413, 2018.
- 1035 Yue, X. and Unger, N.: Ozone vegetation damage effects on gross primary productivity in the  
1036 United States, *Atmos Chem Phys*, 14, 9137-9153, 2014.
- 1037 Yue, X. and Unger, N.: The Yale Interactive terrestrial Biosphere model version 1.0: description,  
1038 evaluation and implementation into NASA GISS ModelE2, *Geosci Model Dev*, 8, 2399-  
1039 2417, 2015.
- 1040 Yue, X., Unger, N., Harper, K., Xia, X., Liao, H., Zhu, T., Xiao, J., Feng, Z., and Li, J.: Ozone  
1041 and haze pollution weakens net primary productivity in China, *Atmos Chem Phys*, 17,  
1042 6073-6089, 2017.
- 1043 Yue, X., Unger, N., Keenan, T. F., Zhang, X., and Vogel, C. S.: Probing the past 30-year  
1044 phenology trend of U.S. deciduous forests, *Biogeosciences*, 12, 4693-4709, 2015.
- 1045 Yue, X., Zhang, T., and Shao, C.: Afforestation increases ecosystem productivity and carbon  
1046 storage in China during the 2000s, *Agr Forest Meteorol*, 296, 108227, 2021.



- 1047 Zhang, Z., Fluet-Chouinard, E., Jensen, K., McDonald, K., Hugelius, G., Gumbrecht, T., Carroll,  
1048 M., Prigent, C., Bartsch, A., and Poulter, B.: Development of the global dataset of Wetland  
1049 Area and Dynamics for Methane Modeling (WAD2M), *Earth System Science Data*, 13,  
1050 2001-2023, 2021.
- 1051 Zhang, Z., Zimmermann, N. E., Stenke, A., Li, X., Hodson, E. L., Zhu, G. F., Huang, C. L., and  
1052 Poulter, B.: Emerging role of wetland methane emissions in driving 21st century climate  
1053 change, *P Natl Acad Sci USA*, 114, 9647-9652, 2017.
- 1054 Zhu, Q., Liu, J., Peng, C., Chen, H., Fang, X., Jiang, H., Yang, G., Zhu, D., Wang, W., and Zhou,  
1055 X.: Modelling methane emissions from natural wetlands by development and application  
1056 of the TRIPLEX-GHG model, *Geosci Model Dev*, 7, 981-999, 2014.
- 1057 Zhuang, Q., Melillo, J. M., Kicklighter, D. W., Prinn, R. G., McGuire, A. D., Steudler, P. A.,  
1058 Felzer, B. S., and Hu, S.: Methane fluxes between terrestrial ecosystems and the  
1059 atmosphere at northern high latitudes during the past century: A retrospective analysis with  
1060 a process-based biogeochemistry model, *Global Biogeochem Cy*, 18, GB3010, 2004.
- 1061  
1062



1063



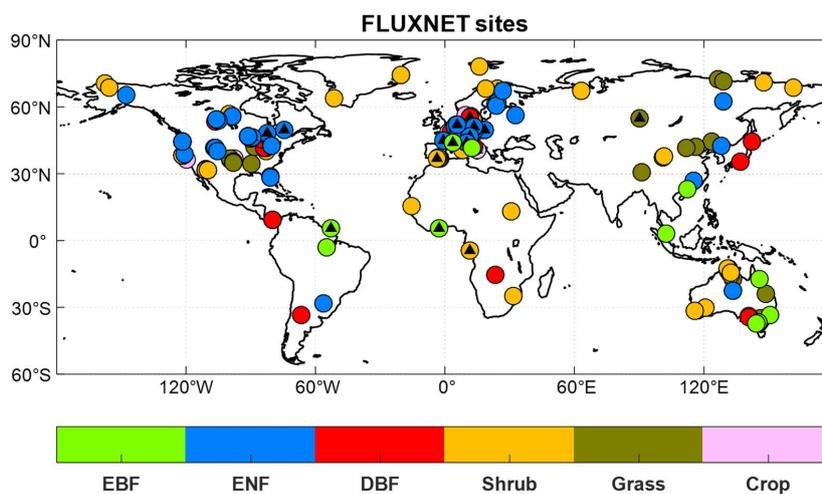
1065

1066 **Figure 1** The illustration of biogeochemical processes in the iMAPLE version 1.0  
 1067 model. The carbon cycle is connected with water cycle, wildfire emissions, biogenic  
 1068 volatile organic compounds (BVOCs) emissions, wetland methane emissions, and is  
 1069 affected by air pollutants including aerosols and ozone. The bold arrows indicate the  
 1070 directions of fluxes and air pollutants. The thin arrows indicate the influential pathways  
 1071 among different components. The dependences on key parameters are shown for some  
 1072 processes. Red fonts indicate new or updated processes in iMAPLE relative to the YIBs  
 1073 model. For detailed parameterizations please refer to section 2.2.

1074

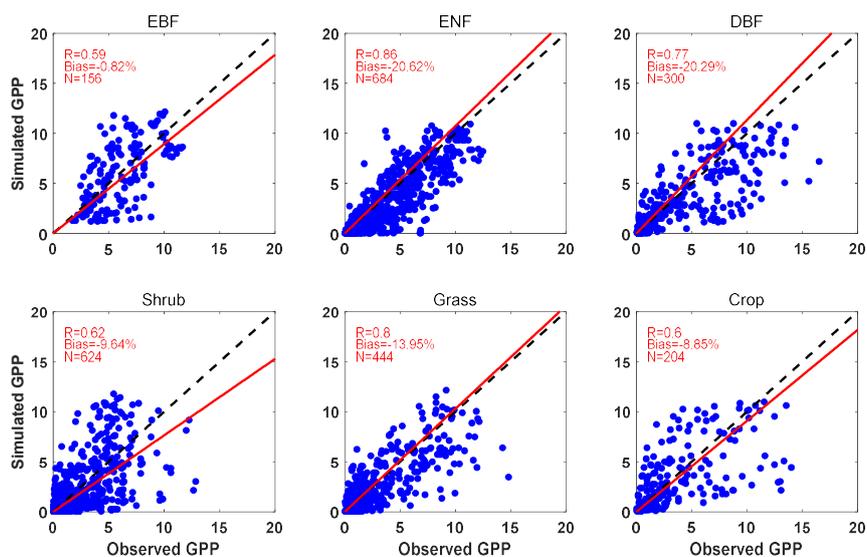
1075

1076



1077  
1078  
1079  
1080  
1081  
1082  
1083  
1084

**Figure 2** Spatial distributions of 201 sites from global FLUXNET network. The colors indicate various plant functional types (PFTs) including evergreen broadleaf forest (EBF, 13 sites), evergreen needleleaf forest (ENF, 57 sites), deciduous broadleaf forest (DBF, 25 sites), Shrub (52 sites), Grass (37 sites), and Crop (17 sites). The black triangles indicate sites with at least one-year observations of diffuse radiation.



1085

1086

1087

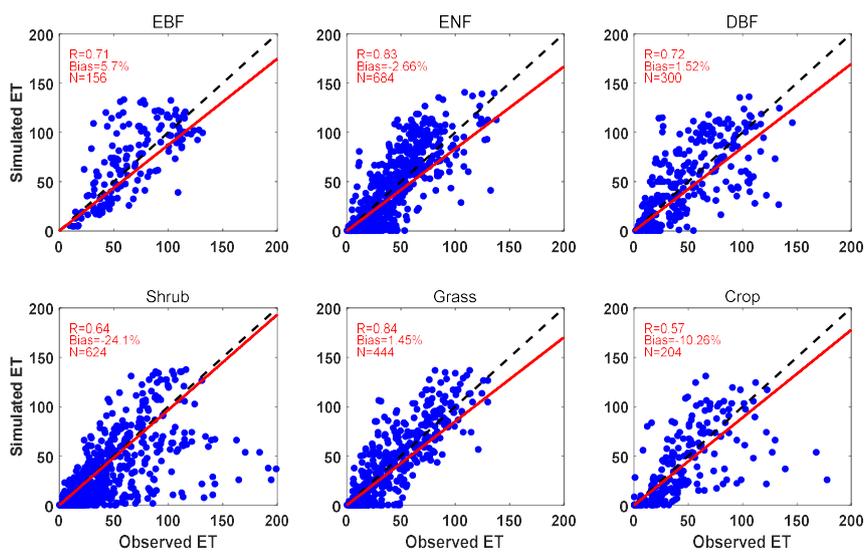
1088

1089

1090

1091

**Figure 3** Comparisons between observed and simulated monthly GPP from 201 FLUXNET sites. Each point indicates the average value of one month at a site. The red line represents linear regression between observations and simulations. The correlation coefficient (R), normalized mean bias and numbers of points/months (N) are shown on each panel. The comparisons are grouped into six PFTs including EBF, ENF, DBF, Shrub, Grass, and Crop. The unit is  $\text{g C m}^{-2} \text{ day}^{-1}$ .



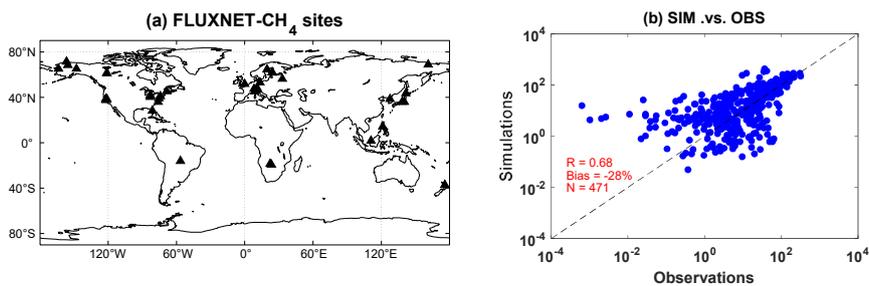
1092

1093

1094

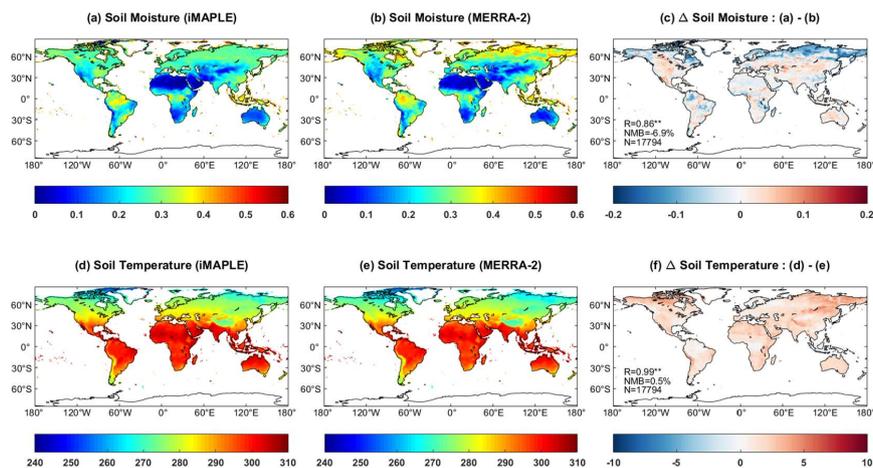
1095

**Figure 4** The same as Figure 3 but for ET. The unit is mm month<sup>-1</sup>.



1096  
1097  
1098  
1099  
1100  
1101  
1102

**Figure 5** Spatial distribution of global FLUXNET-CH<sub>4</sub> sites and comparisons between observed and simulated monthly methane flux. Filled triangles indicate sites with at least six months observations of wetland CH<sub>4</sub> fluxes. Each point represents average value of monthly methane emission at one site. The correlation coefficient (R), normalized mean bias and numbers of points/months (N) are shown on the right panel. The unit is g [CH<sub>4</sub>] m<sup>-2</sup> yr<sup>-1</sup>.



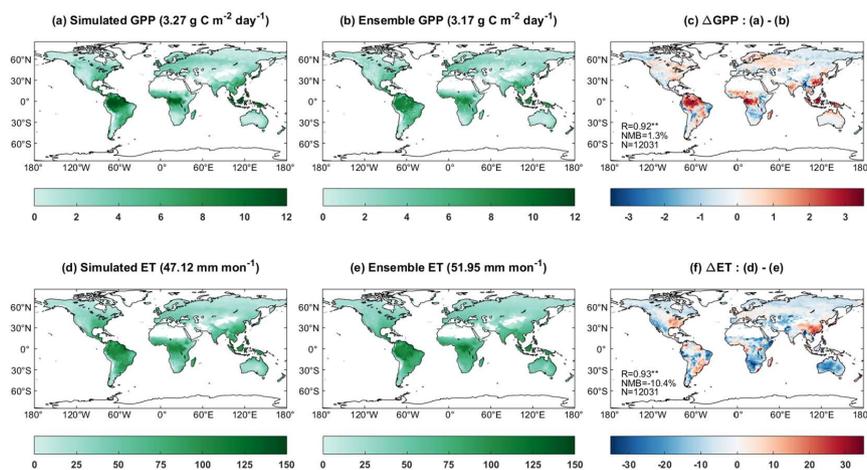
1103

1104 **Figure 6** Comparisons of simulated (a) soil moisture ( $\text{m}^3 \text{m}^{-3}$ ) and (d) soil temperature (K) from the  
1105 iMAPLE model with (b, e) the MERRA-2 reanalyses. Both simulations and observations are  
1106 averaged for the period of 1980-2020. The spatial difference, correlation coefficient (R), normalized  
1107 mean bias (NMB) between simulations and observations and numbers of points (N) are shown on  
1108 (c) and (f), respectively.

1109

1110

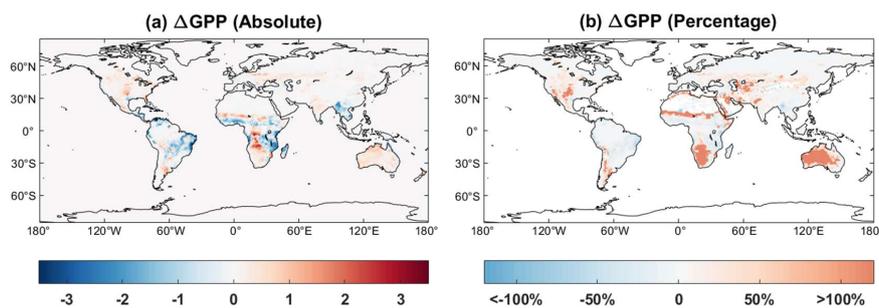
1111



1112

1113 **Figure 7** Comparisons of simulated (a) gross primary productivity (GPP, g C m<sup>-2</sup> day<sup>-1</sup>) and (d)  
1114 evapotranspiration (ET, mm month<sup>-1</sup>) with ensemble products from (b, e) observations. Simulated  
1115 GPP and ET are performed by iMAPLE driven with meteorology from MERRA-2 reanalysis during  
1116 2001-2013. Ensemble GPP products are from the average values of SIF-based GOSIF and satellite-  
1117 based GLASS GPP products. Ensemble ET products include FLUXCOM and GLASS products  
1118 during 2001-2013. The spatial difference, correlation coefficient (R), normalized mean bias (NMB)  
1119 between simulations and observations and numbers of points (N) are shown on (c) and (f). Only  
1120 land grids with vegetation are shown on each panel, and their area-weighted values are shown in  
1121 titles.

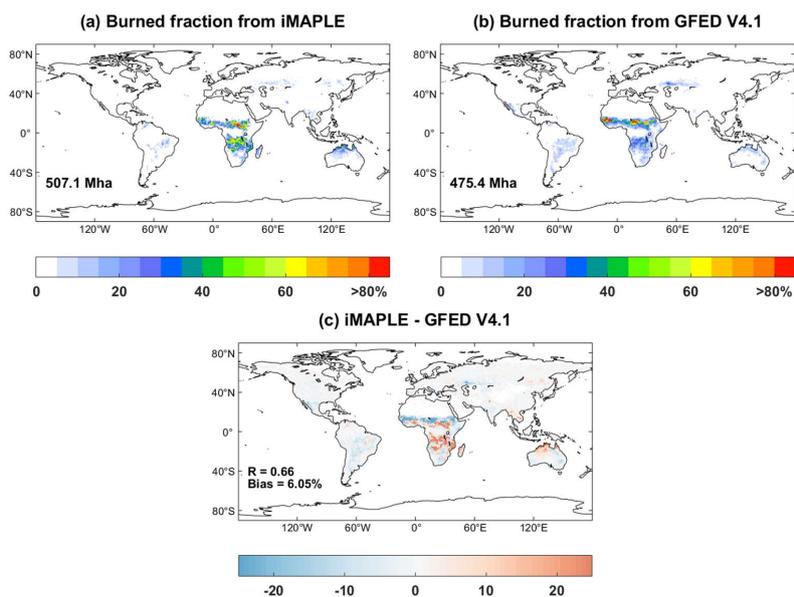
1122



1123

1124 **Figure 8** Absolute ( $\text{g C m}^{-2} \text{ day}^{-1}$ ) and relative (%) differences of global GPP between simulations  
1125 with and without two-way carbon-water coupling processes. Simulation results are averaged for the  
1126 period of 1980-2020.

1127



1128

1129 **Figure 9** Comparisons of global burned fraction (%) between (a) simulations and (b) observations.

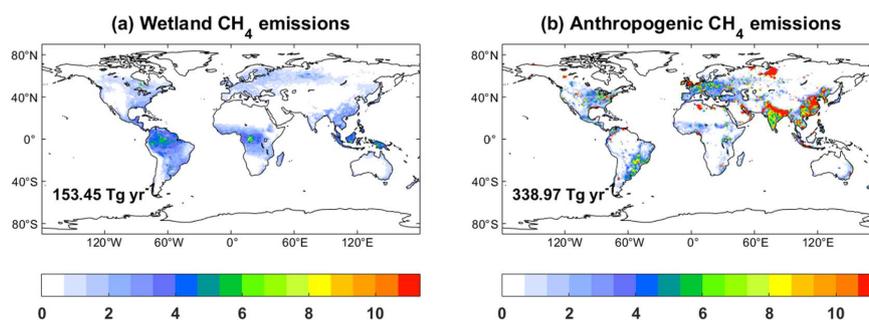
1130 Simulations are performed using iMAPLE and observations are from GFED V4.1 fire emissions

1131 products. Both simulations and observations are averaged for the 1997-2016 period. The global total

1132 area burned are shown on (a) and (b). The spatial difference, correlation coefficient (R), and

1133 normalized mean biases between simulations and observations are shown on (c).

1134



1135

1136

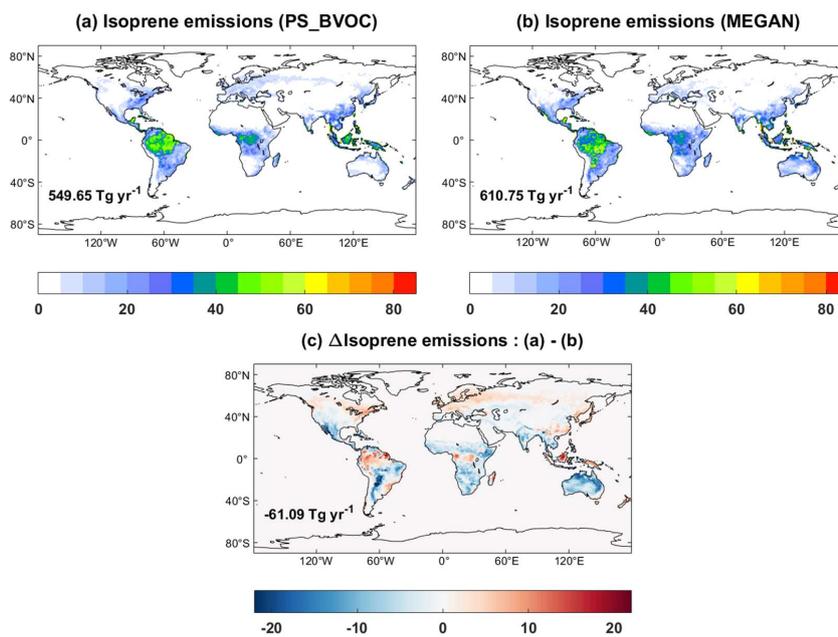
1137

1138

1139

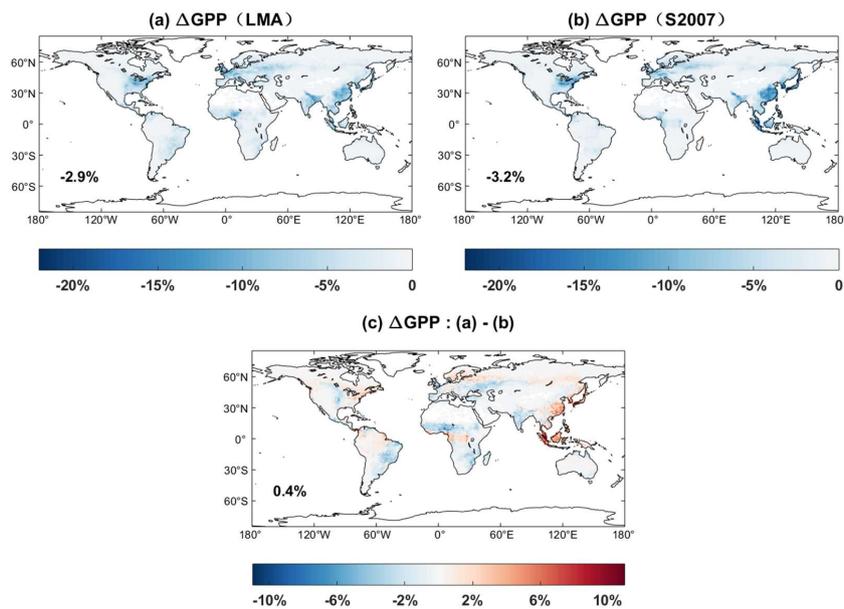
1140

**Figure 10** Global CH<sub>4</sub> emissions (g [CH<sub>4</sub>] m<sup>-2</sup> yr<sup>-1</sup>) from (a) wetland and (b) anthropogenic sources. Anthropogenic sources include energy, agriculture, industrial, residential, shipping, solvent and transportation. The global total emissions are shown on each panel. Both the wetland and other emissions are averaged for 2000-2014.



1141  
1142  
1143  
1144

**Figure 11** Global isoprene emissions ( $\text{mg C m}^{-2} \text{ day}^{-1}$ ) from (a) MEGAN, (b) PS\_BVOC schemes and (c) their differences. The global total emissions are shown on each panel.



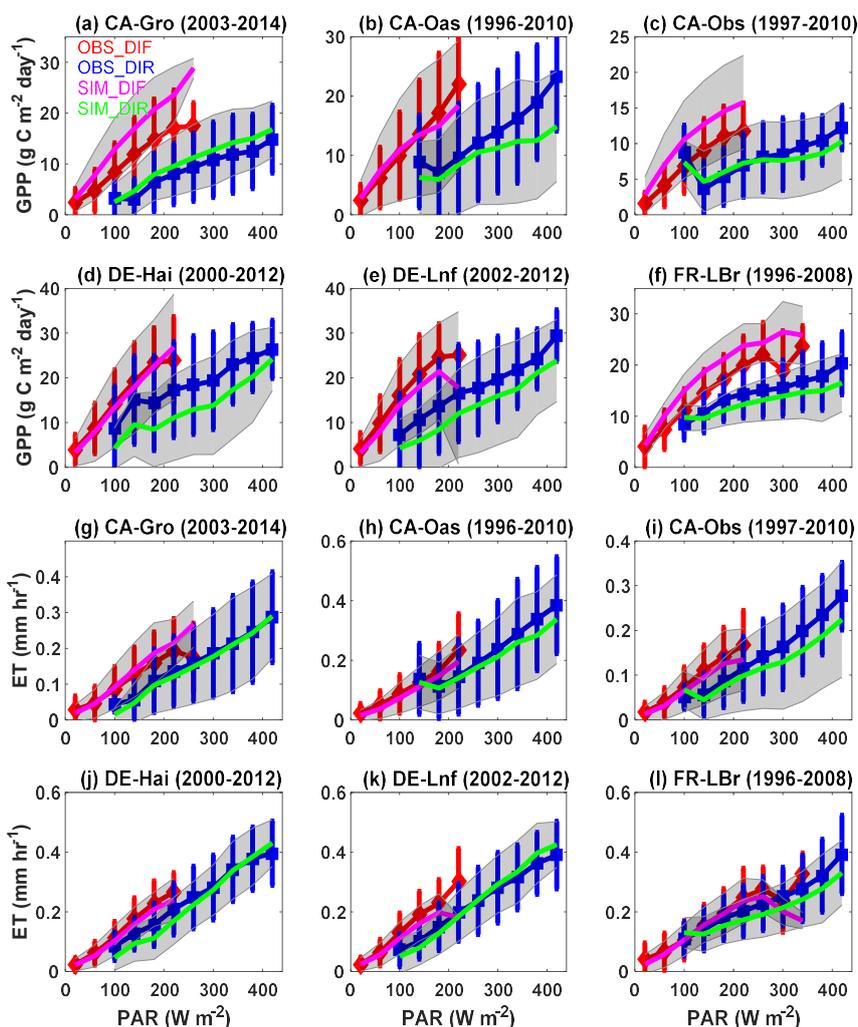
1145

1146 **Figure 12** Percentage changes of global GPP caused by ozone damage effects. The ozone damage  
1147 schemes include (a) trait leaf mass per area (LMA)-based, (b) S2007 plant ozone sensitivity and (c)  
1148 their differences.

1149

1150

1151



1152  
1153 **Figure 13** Observed and simulated responses of site-level (a-f) GPP and (g-l) ET to diffuse and  
1154 and direct radiation at the FLUXNET sites. Photosynthetically active radiation (PAR) reaching the  
1155 surface are divided into diffuse (diffuse fraction > 0.75) and direct (diffuse fraction < 0.25)  
1156 radiation at six FLUXNET sites with more than 10 years of observations. Observations (simulations)  
1157 are grouped over PAR bins of 40 W m<sup>-2</sup> with errorbars (shadings) indicating standard deviations of  
1158 GPP and ET for each bin. The red (blue) and magenta (green) represent observed and simulated  
1159 responses of GPP and ET to diffuse (direct) radiation. Units of GPP and ET are g C m<sup>-2</sup> day<sup>-1</sup> and  
1160 mm hr<sup>-1</sup>, respectively.  
1161